Volume 45
DOE/DP40200-149

# LLE Review

## Quarterly Report

## October–December 1990

Laboratory for Laser Energetics
College of Engineering and Applied Science
University of Rochester
250 East River Road
Rochester, New York 14623-1299

Volume 45
DOE/DP40200-149

# LLE Review

## Quarterly Report

*Editor:* E. M. Epperlein
(716) 275-8245

## October–December 1990

Laboratory for Laser Energetics
College of Engineering and Applied Science
University of Rochester
250 East River Road
Rochester, New York 14623-1299

This report was prepared as an account of work conducted by the Laboratory for Laser Energetics and sponsored by Empire State Electric Energy Research Corporation, New York State Energy Research and Development Authority, Ontario Hydro, the University of Rochester, the U.S. Department of Energy, and other United States government agencies.

# IN BRIEF

This volume of the LLE Review, covering the period October–December 1990, contains descriptions of a new phase-conversion technique designed to improve irradiation uniformity, a report on the interpretation of high-density implosion experiments of argon-filled targets, and an article on the use of absorption spectroscopy to diagnose compressed target layers. The section on advanced technology has a report on the application of KTP crystals as electro-optic amplitude modulators, and describes the use of chirped-pulse technology to measure $\chi^{(3)}$ by nearly degenerate four-wave mixing. Finally, the activities of the National Laser Users Facility and the GDL and OMEGA laser facilities are summarized.

The highlights of this issue are

- A new phase-conversion technique based on distributed polarization rotation has been developed to provide instantaneous smoothing of the intensity nonuniformities at the target plane.

- The one-dimensional hydrodynamic code *LILAC*, which includes an average-ion model, has been used to interpret the core conditions of high-density implosions of argon-filled polymer shell targets.

- The effect of temperature dependence of x-ray absorption features on the interpretation of target implosions has been investigated.

- An experimental study of KTP Pockels cells has demonstrated their use in both YLF regenerative amplifiers and Q-switched laser systems.
- Picosecond, chirped-pulse technology has been used to generate two spectrally separate, time-synchronized pulses for $\chi^{(3)}$ measurements by nearly degenerate four-wave mixing.

# CONTENTS

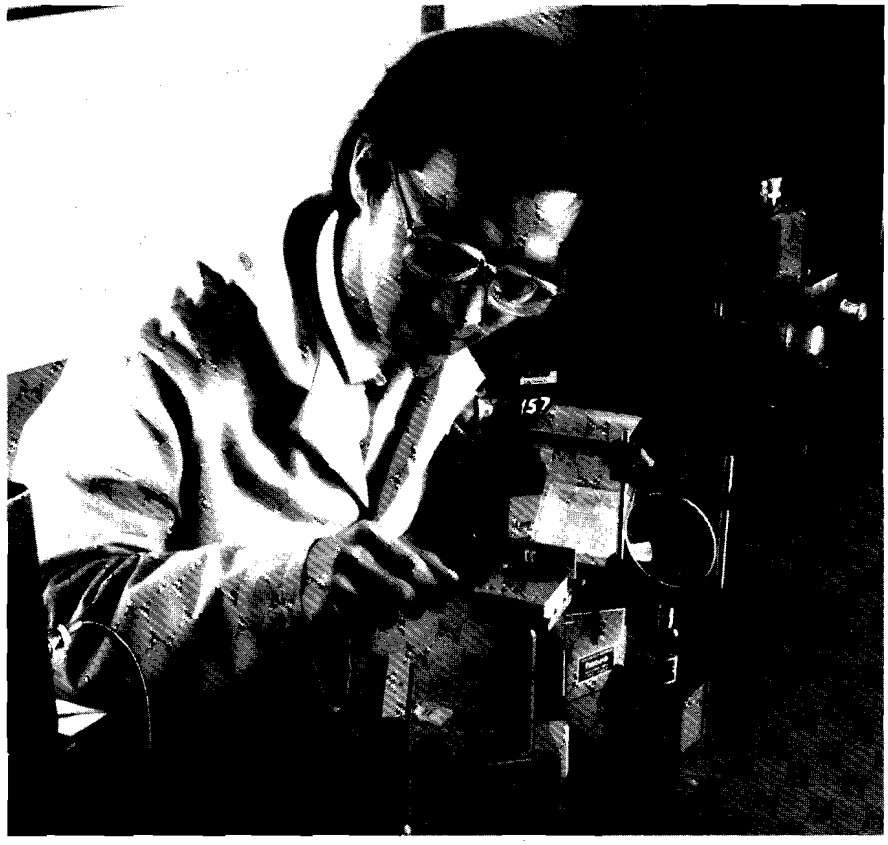

Yung-Ho Chuang, Graduate Research Fellow, is shown adjusting the spectral windowing mask that allows the production of spectrally distinct laser pulses used in the measurement of the nonlinear index of refraction of materials.

# Section 1
# PROGRESS IN LASER FUSION

## 1.A Phase Conversion Using Distributed Polarization Rotation

An essential requirement for direct-drive laser fusion is the uniform irradiation of fuel pellets located in the quasi far field of a multibeam laser system. To achieve the high-density compressions required for high-gain thermonuclear fusion, the implosion of the target fuel must be highly symmetric. More precisely, nonuniformities in the radiation pressure should not exceed 1% or 2%. To achieve this level of uniformity, not only accurate pointing, focusing, timing, and energy balance of the individual beams are required, but, more importantly, each of the laser beams must have a uniform focal-intensity distribution.

The intensity nonuniformities are caused by spatial variations in the near-field phase front of each laser beam.[1] Phase error, caused by variations in both geometrical path length and refractive index, is accumulated throughout each beamline. The frequency conversion of infrared light to ultraviolet light results in a tripling of beam phase error, causing larger intensity variations for ultraviolet light. This limits the level of irradiation uniformity that can be obtained by coherently focusing a laser beam. However, by modifying the phase or coherence properties of the laser beam, thereby changing its focusing characteristics, the level of irradiation uniformity can be improved. The method of induced spatial incoherence[2,3] (ISI) involves a reduction in both spatial and temporal coherence. Other approaches, such as random phase plates and lens arrays, are based on static spatial phase modulation of a laser beam.[4,5] The Laboratory for Laser Energetics has proposed a number of phase-conversion schemes, combining spatial phase

modulation with temporal phase modulation of a laser beam to demonstrate uniform, frequency-tripled laser radiation at the target plane.[6–9]

In the case of spatial phase conversion alone, the laser-plasma interaction physics is expected to differ from that with ideal target irradiation because of the stationary intensity fluctuations associated with a multibeamlet interference pattern. Generally, the short-wavelength interference structures that are 1% of the target diameter are assumed to be smoothed by thermal conduction in the plasma. However, it is currently unknown whether the detailed power spectrum of the phase-converted radiation, being shifted to shorter scale-length-intensity fluctuation, is more or less likely to "seed" the Rayleigh-Taylor hydrodynamic instability. Also, a high-intensity speckle in the laser can locally reduce the coronal plasma density, thereby increasing the refractive index and giving rise to self-focusing. The resulting breakup of the beam into self-focused filaments can then induce nonuniformities in the ablation pressure, as well as parametric instabilities.

Phase-conversion schemes involving broadband laser radiation, such as smoothing by spectral dispersion (SSD), can potentially reduce the likelihood of both filamentation and Rayleigh-Taylor instabilities, thereby providing the levels of irradiation uniformity required for ignition-scaling experiments. To improve the compression symmetry, the time interval for speckle shift must be short compared to the hydrodynamic response time of the plasma. High-peak-power Nd:glass lasers can, in principle, be operated with sufficient bandwidth to satisfy this requirement. However, the need for frequency tripling on OMEGA introduces certain constraints. For efficient frequency tripling, proper phase matching of broadband (~10-Å) light demands the use of infrared and ultraviolet diffraction gratings. Since large-aperture gratings of high damage threshold are not yet available, we are currently exploring alternative techniques designed to reduce the instantaneous level of irradiation nonuniformity on target.

One of the new phase-conversion techniques involves the use of beam-polarization segmentation, in conjunction with distributed phase plates (DPP's), such as those used on OMEGA. The effectiveness of this scheme has already been experimentally demonstrated by placing a half-wave retardation plate into half of a phase-converted laser beam. This resulted in significant reduction in speckle contrast over all spatial modes. More recently, a prototype distributed polarization rotator (DPR) has been fabricated and tested.[10] A time-instantaneous increase in irradiation uniformity has been likewise demonstrated using the DPR. In addition, by setting the polarization cycling to complement the color cycling produced by SSD, the time-dependent uniformity can be optimized.

In this article we first review the theory of speckle statistics, with which predictions of instantaneous speckle smoothing are obtained. Secondly, we describe the design of the DPR, highlighting the details of polarization, propagation, and interference. Lastly, we describe several experimental demonstrations, comparing them with the theoretical predictions.

### Theory of Speckle Statistics

In general, phase conversion of laser light utilizes both spatial and temporal phase modulation to smooth the intensity distribution at the target plane. Schematically illustrated in Fig. 45.1, characteristics of the target-plane profile are determined by the size and distribution of elements within an optical array, such as a DPP. Time-varying phase and spatial phase modulation are used to smooth the resulting speckle distribution. The expression for two-beam interference is given by

$$I = I_1 + I_2 + [\boldsymbol{a}_1 \cdot \boldsymbol{a}_2]\,\mu_{12}(t)\,[I_1 I_2]^{1/2} \cos[(\omega_1 - \omega_2)t + (\phi_1 - \phi_2)], \quad (1)$$

where $\boldsymbol{a}$ is the polarization vector, $I$ is the resulting intensity, $\omega$ is the angular frequency, and $\phi$ is the relative phase. Each of these parameters can be made to vary in space or time to smooth the interference pattern. Referring to Eq. (1), it is evident that incoherent addition of array elements is achieved when polarization vectors are orthogonal, causing the modulation term in the interference pattern to be zero and thus reducing the speckle contrast to zero. This is the basis for beam smoothing through polarization distribution. Correlation control between the spatial polarization segmentation, the DPP mask, and SSD color cycling provides additional smoothing mechanisms, but these mechanisms are not described in this article.

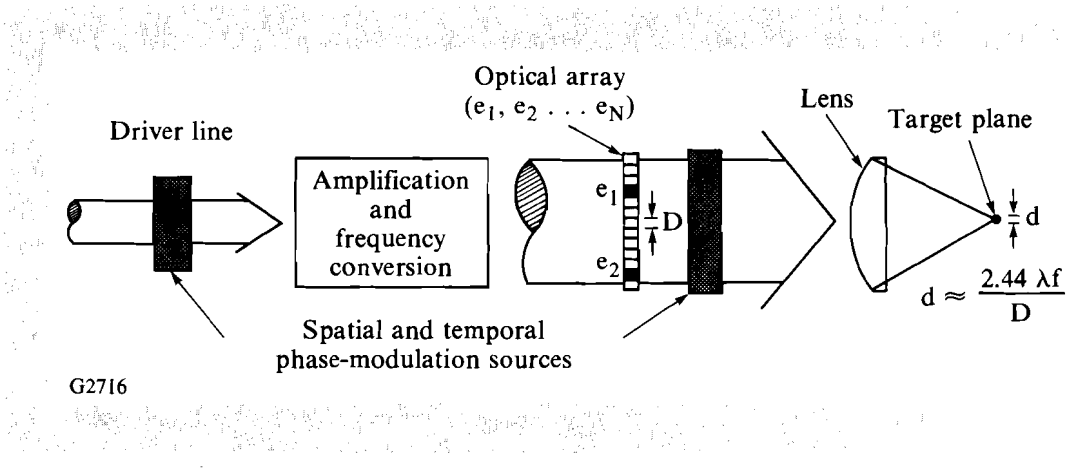


Fig. 45.1
Phase conversion of laser light, utilizing both spatial and temporal phase modulation, smooths the intensity distribution at the target plane. Spatial characteristics of the target-plane profiles are determined by an optical array placed before the focused lens; time-dependent phase, applied in the driver line, and additional spatial phase modulation, applied after frequency conversion, are used to smooth the resulting speckle distribution. Incoherent addition of array elements, instantaneously achieved when $\boldsymbol{a}_1 \cdot \boldsymbol{a}_2 = 0$ (i.e., $\boldsymbol{a}_1$, $\boldsymbol{a}_2$ are orthogonal), reduces speckle contrast.

A DPP is composed of an ordered array of transparent elements where the lateral dimension of each element is chosen to be small compared to the size of the phase and amplitude disturbances in the initial laser beam. Phase retardation is randomly distributed in an array of hexagons, each adding a phase delay of either 0 or $\pi$ radians.

Collimated laser light transmitted through the DPP is broken into coherent, phase-retarded beamlets and brought to focus, where a superposition of beamlets is formed. Although the overlapped beamlets interfere to produce large intensity modulations at the target plane, with 10,000 beamlets per plate, the envelope of the focal distribution is a smooth distribution determined by the diffraction pattern of the individual area elements of the DPP and the detailed correlations between the DPP mask and the laser beam.

The amplitude distribution at the Fourier transform (focal) plane is given by

$$A(\varepsilon,\eta) = \int_{-\infty}^{\infty}\int a(\alpha_1,\beta_1)e^{-2\pi i(\alpha_1\varepsilon+\beta_1\eta)}\,d\alpha_1\,d\beta_1\,, \tag{2}$$

where $a(\alpha_1,\beta_1)$ is the complex amplitude distribution, $\varepsilon = \alpha_2/\lambda f$ and $\eta = \beta_2/\lambda f$ are the spatial-frequency variables, $\lambda$ is the wavelength of light, and $f$ is the focal length. The input amplitude is a product of the laser-beam amplitude (denoted by $L$) and the amplitude transmittance of the DPP.[6] The amplitude distribution $A(\varepsilon,\eta)$ can be conveniently expressed as

$$A(\varepsilon,\eta) \propto A_L(\varepsilon,\eta) \otimes \left[\frac{J_1(\pi d_o \omega)}{\pi d_o \omega}\right]\left[\sum_{j=1}^{N}\sum_{k=1}^{N} e^{2\pi i\left(\varepsilon\alpha_i+\eta\beta_K+\frac{\phi_{R_{j,k}}}{2\pi}\right)}\right]. \tag{3}$$

The random variable $\phi_{R_{j,k}}$ represents the phase retardation of the $(j,k)^{th}$ element (of size $d_o$).

The square of the envelope function $J_1(x)/x$, known as the Besinc function, where

$$\omega = \sqrt{\varepsilon^2+\eta^2}$$

represents the slowly varying profile of the focal intensity distribution $I(\varepsilon,\eta)$. The convolution in Eq. (3) (denoted by $\otimes$), between the far-field amplitude distribution of the laser beam $A_L(\varepsilon,\eta)$ and the product of a low-frequency envelope and a superposition of random spatial-frequency harmonics, is responsible for the detailed power spectrum of the resulting intensity distribution.

This intensity distribution is often referred to as laser speckle. Analysis of a speckle distribution can be performed using the classical model for random walk in the complex plane.[11] Using this approach, the statistical description of the amplitude distribution in Eq. (3) may be written as follows:

$$A(x,y,z) = \sum_{k=1}^{N}\frac{1}{\sqrt{N}}a_k(x,y,z) = \frac{1}{\sqrt{N}}\sum_{k=1}^{N}a_k e^{i\phi_k}\,, \tag{4}$$

where $a_k$ and $\phi_k$ are assumed to be statistically independent for all $k$, and $\phi_k$ is uniformly distributed over $(-\pi, \pi)$.

Taking the limit of a large number of independent variables $N$ and using the central limit theorem, it can be shown that the normalized probability-density function $P_1(I)$ of the intensity corresponding to one speckle pattern is given by

$$P_1(I) = \begin{cases} \frac{1}{\bar{I}} e^{-I/\bar{I}} & I \geq 0 \\ 0 & I < 0 \end{cases} , \tag{5}$$

where $\bar{I}$ is the average intensity.

The DPR, together with the DPP, produces two orthogonally polarized speckle patterns. The speckle patterns can be added on the basis of intensity since the modulation term of the interference pattern goes to zero as $\boldsymbol{a}_1 \cdot \boldsymbol{a}_2 = 0$. The normalized probability-density function $P_2(I)$ resulting from the intensity addition of two uncorrelated, but equally weighted, speckle patterns has also been derived in Ref. 11 and shown to be

$$P_2(I) = \frac{4I}{\bar{I}^2} e^{-2I/\bar{I}} . \tag{6}$$

The contrast associated with each speckle distribution, defined by

$$c \equiv \frac{\sqrt{\overline{I^2} - \bar{I}^2}}{\bar{I}} , \tag{7}$$

is found to be $\sqrt{2}$ smaller for the case of two speckle patterns added on the basis of intensity.

A simple explanation for the decrease in contrast can be given by examining the intensity probability-density curves plotted in Fig. 45.2. Curve $P_1$ shows that a limited number of high-intensity speckles are distributed within a large number of regions having zero intensity. The highest

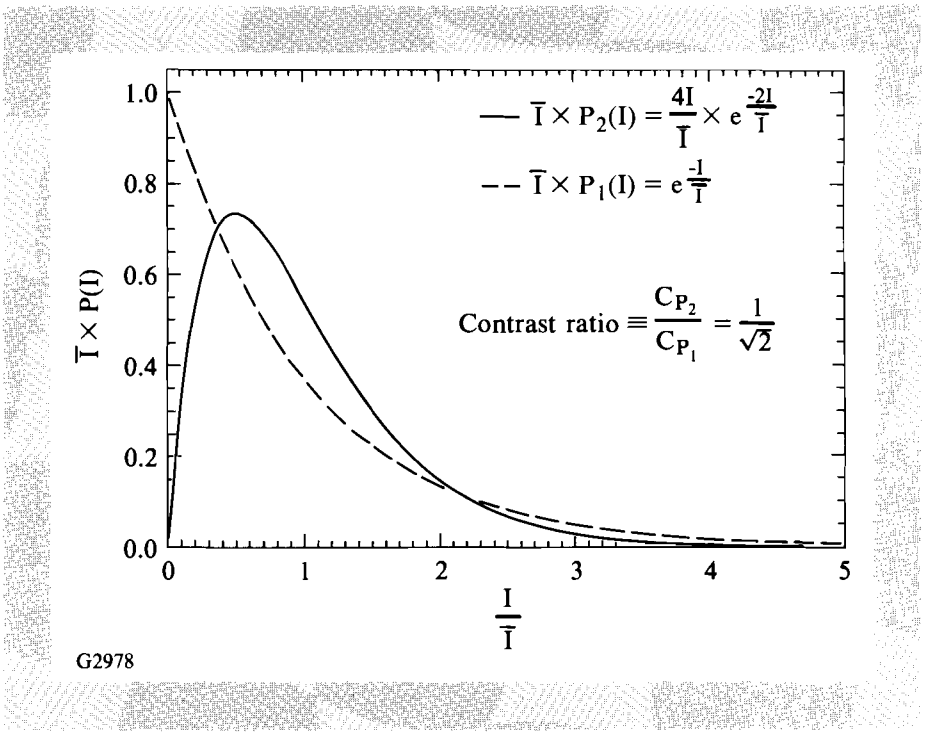


Fig. 45.2
The intensity probability-density function of one polarized, random speckle pattern obeys negative exponential statistics as shown in curve $P_1(I)$. Two speckle patterns, added on the basis of intensity, exhibit different intensity statistics as shown in curve $P_2(I)$. A greater number of intensity values falls near the mean intensity, the probability of higher intensity decreases, and the resulting speckle contrast is reduced by $\sqrt{2}$.

probability is for zero intensity. It is reasonable to expect that, for two uncorrelated distributions, the probability of exact overlap of the highest-intensity speckles is extremely low. Therefore, the number density of high-intensity speckles approximately doubles, the mean intensity doubles, but the value of the individual peaks remains the same. The probability-density function $P_2$, resulting from the incoherent addition of two speckle distributions, is also shown in Fig. 45.2. A decrease in speckle contrast is observed as an increase in the number of intensity values polling near the mean intensity. This decrease also applies to the addition of two orthogonally polarized and uncorrelated speckle patterns, since they effectively add on an incoherent basis. The greatest time-instantaneous improvement is obtained when the intensity peaks of one polarization fill the zeros of the orthogonal polarization at the transform plane. Correlation control of the phase mask can potentially optimize this effect for a particular DPR configuration.

## Design of the DPR

The DPR is a wedged wave plate constructed from a birefringent fluid. As shown in Fig. 45.3(a), a nematic liquid-crystal fluid fills the volume within the wedge formed by two plane-parallel substrates. The birefringence varies linearly along the wedge as described by

$$\Gamma = t(y)\Delta n \ , \tag{8}$$

where $\Gamma$ is the optical path difference between orthogonal polarizations, $t$ is the path in the liquid crystal, and $\Delta n$ is the birefringence of the fluid. The DPR transforms an incident linearly polarized beam into two orthogonally polarized beams. The incoming light is linearly polarized parallel to the DPR

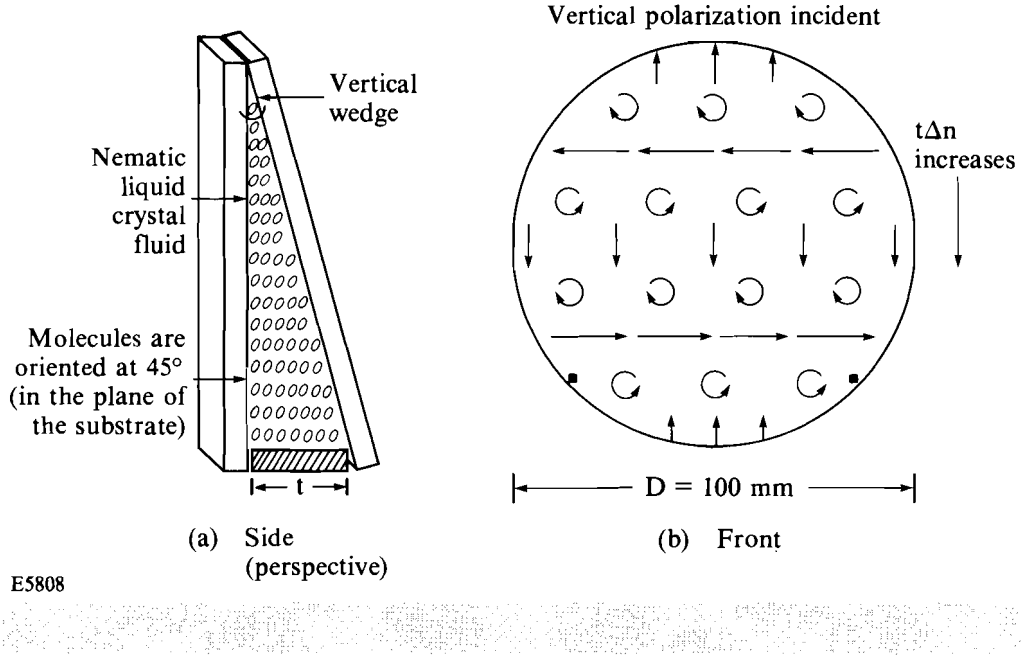


Fig. 45.3
The distributed polarization rotator (DPR) is an optical device that converts one polarized beam into two orthogonally polarized beams. The wedged DPR is a continuously varying wave plate that produces two co-propagating, orthogonally polarized, complementary interference patterns. A nematic liquid crystal fills a wedge formed between two parallel plates [Fig. 45.3(a)], yielding enough retardance to produce several polarization cycles along one dimension of the beam [Fig. 45.3(b)].

wedge angle. The fast and slow axes of the liquid crystal are oriented at ±45° to the wedge. The polarization of the transmitted light varies continuously for several cycles along the vertical dimension, as shown in Fig. 45.3(b).

Liquid-crystal DPR's are made in a manner similar to the fabrication of liquid-crystal polarizers and wave plates.[12] A polymer alignment layer is coated onto the inner surface of each substrate. This layer is unidirectionally rubbed at 45° with respect to the wedge angle formed by the two spacers [see Fig. 45.4(a)]. A 100-μm spacer is used to produce one milliradian of wedge. A nematic liquid crystal fills the wedge volume with the molecules anchored to the alignment layer, producing a molecular arrangement similar to that of a uniaxial crystal. The liquid-crystal fluid is a blend of saturated nematics, which are chosen to yield high-UV transmission and high damage threshold.[13] Figure 45.4(b) shows the molecular structure of the fluid and summarizes the performance criteria for which it was chosen as the optimum DPR material. The damage threshold of the saturated nematic blend surpasses requirements for both OMEGA and the proposed upgrade to OMEGA. Light transmission at $\lambda = 0.351$ μm is greater than 99% and is limited only by the quality of antireflection coating on the substrates and by the degree of index mismatch at the fluid-to-polymer and polymer-to-substrate interfaces.

Fig. 45.4
The DPR consists of two parallel plates, a polymer alignment layer and a thin layer of nematic liquid crystal [Fig. 45.4(a)]. The liquid-crystal molecules, anchored to a unidirectionally rubbed polymer film, exhibit uniaxial crystalline behavior. A blend of saturated nematics maximizes UV-laser-damage resistance and UV transmission. Liquid-crystal birefringence and the DPR wedge angle determine the polarization cycling rate illustrated in Fig. 45.3(b).

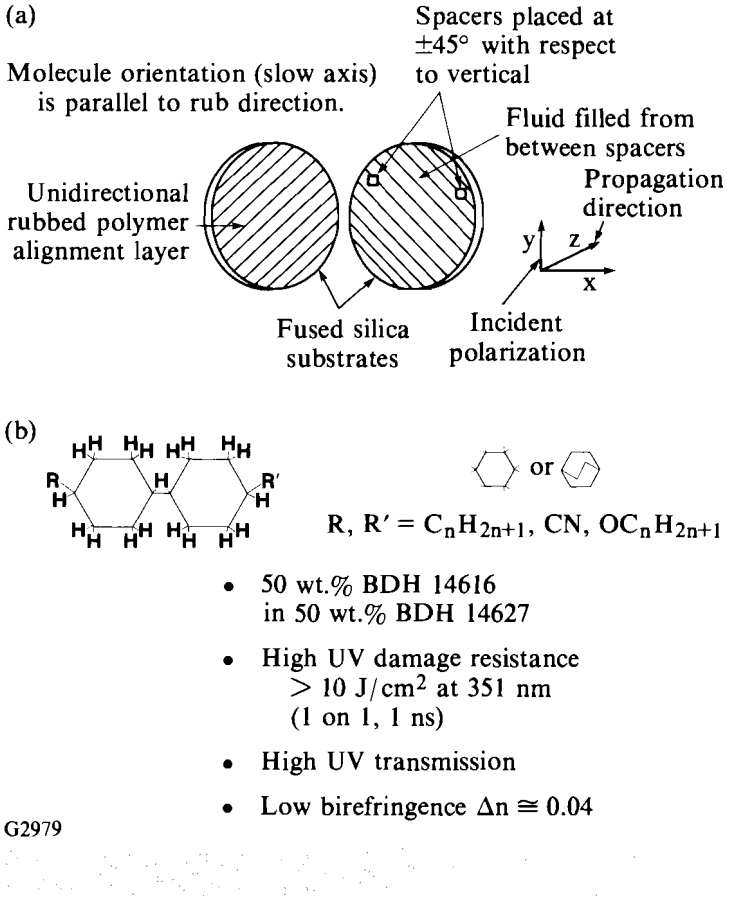

The wedged DPR is a continuously varying wave plate. The two polarizations produced are along the $n_e$ and $n_o$ axes (fast and slow axes, respectively) of the DPR. These directions are parallel and perpendicular to the rub direction or ±45° with respect to the wedge and the incident-light polarization. The ordinary and extraordinary components of the incident light experience unequal optical-path difference, again varying linearly in the vertical direction. These components of light experience a different wedge through the DPR and are tilted by a differential angle $\Delta\alpha_w$ given by

$$\Delta\alpha_w = \frac{t\Delta n}{D}, \tag{9}$$

where $D$ is the DPR diameter, $\Delta n$ is the birefringence, and $t$ is the spacer thickness.

It is important that an angle exist between the two polarization components, since both components carry the same dephasing structure as they exit the DPP. Since each of these polarizations samples the whole phase plate, it is not correct to assume that the two speckle patterns are uncorrelated. In fact, they are strongly correlated but travel with different $\boldsymbol{k}$ vectors. This means that there exists a displacement between the two speckle fields. They are not registered exactly in space, but rather they are separated by a short correlation interval. Since this example does not satisfy the theoretical assumption of uncorrelated intensity addition, it is reasonable to expect that improvements in contrast would be greater for spatial frequencies closest in value to this correlation interval. Careful analysis of the speckle data is required. Results of such analysis are contained in the experimental section.

Another way of describing light transmitted through a DPR is based on polarization components that are parallel and perpendicular to the incident beam. In this case, the DPR is said to have produced two co-propagating, orthogonally polarized, complementary interference patterns. This perspective is completely consistent with the explanation involving angularly separated components since the grating angle is found to be equivalent to the differential-refraction angle as shown by

$$\theta_D = \lambda/d = \theta_R = d'/f, \tag{10}$$

where $\theta_D$ is the required grating angle of interference, $\theta_R$ is the differential-refraction angle (i.e., the angular separation of the two polarization components), $d$ is the spacing of full-wave retardation or half-wave average phase delay, $d'$ is the linear separation of the speckle pairs in the target plane, and $f$ is the focal length of the targeting lens.

**Experimental Demonstration**

The DPR is placed within a two-dimensional, imaging, UV polariscope to demonstrate high-contrast polarization cycling. An argon-ion laser, operating at $\lambda = 351$ nm with vertical polarization, was used as the light source for the polariscope. One of two interference patterns transmits through the

analyzer to the imaging system as shown on the left side of Fig. 45.5. The vertical-line profile on the right shows high-contrast modulation, thus demonstrating high-polarization purity.

A far-field detection system images the light transmitted through the DPP and DPR (see Fig. 45.6). The profile at the left shows an intensity cross section from the DPP pattern, while the profile at the right shows an intensity cross section from the combination of a DPP and DPR. The azimuthal averages of the speckle profile show the characteristic envelope from the DPP hexagons. The contrast of speckle modulation is reduced by an amount greater than $\sqrt{2}$. This is seen by observing that the ratio of peak intensity to average intensity decreases with a DPR.

The individual intensity values of the measured speckle patterns are sorted to form the frequency function, referred to in the theory section as probability-density function. Referring to Fig. 45.7, the measured, non-DPR curve is shifted to the right of the theoretical, non-DPR curve. This is caused by a diagnostic limitation preventing correct measurement of intensity values near zero. Since this error is systematically present in all measurements, it is the ratio of speckle contrast that is important to assess the performance of the DPR. The measured contrast ratio with and without the DPR is greater than $\sqrt{2}$.

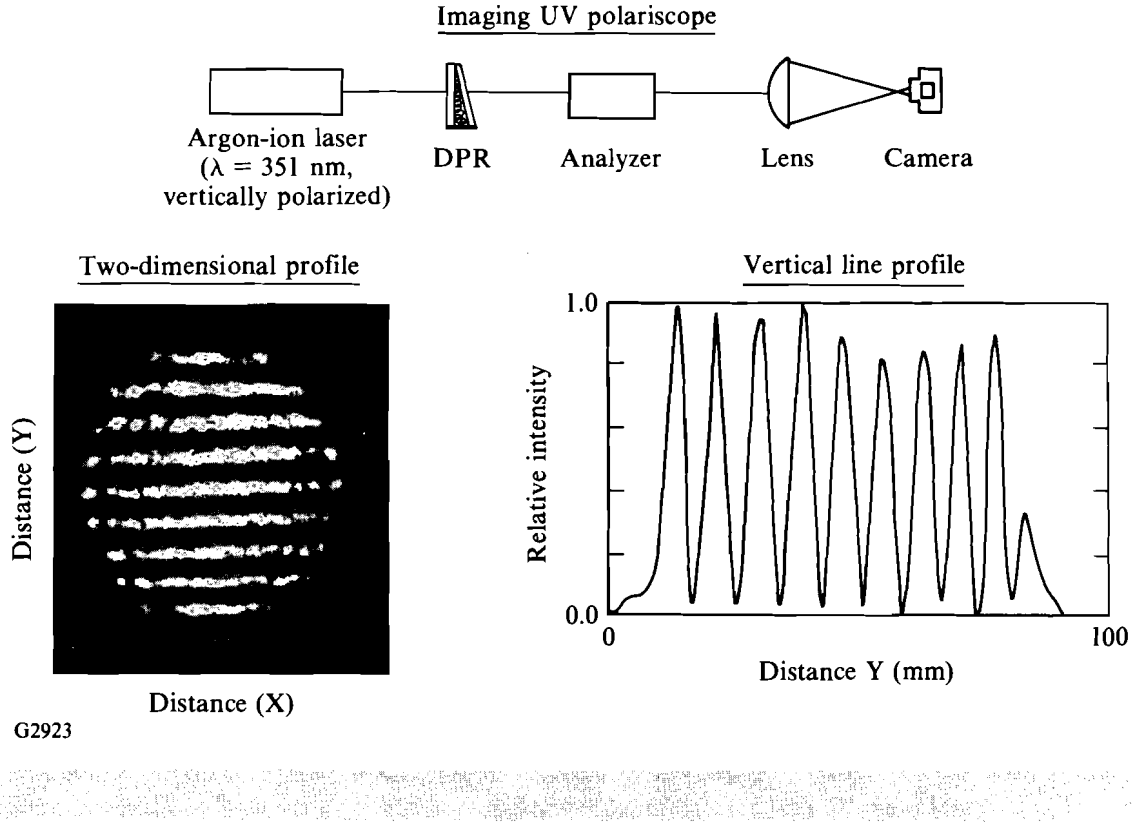


Fig. 45.5
The wedged DPR produces high-contrast, complementary interference patterns. The DPR is placed within a two-dimensional, imaging, ultraviolet polariscope to demonstrate high-contrast polarization cycling. One of two interference patterns transmits through the analyzer to the imaging system. The contrast of the sinusoidal intensity distribution, shown by the vertical line profile, is directly related to the purity of polarization cycling.

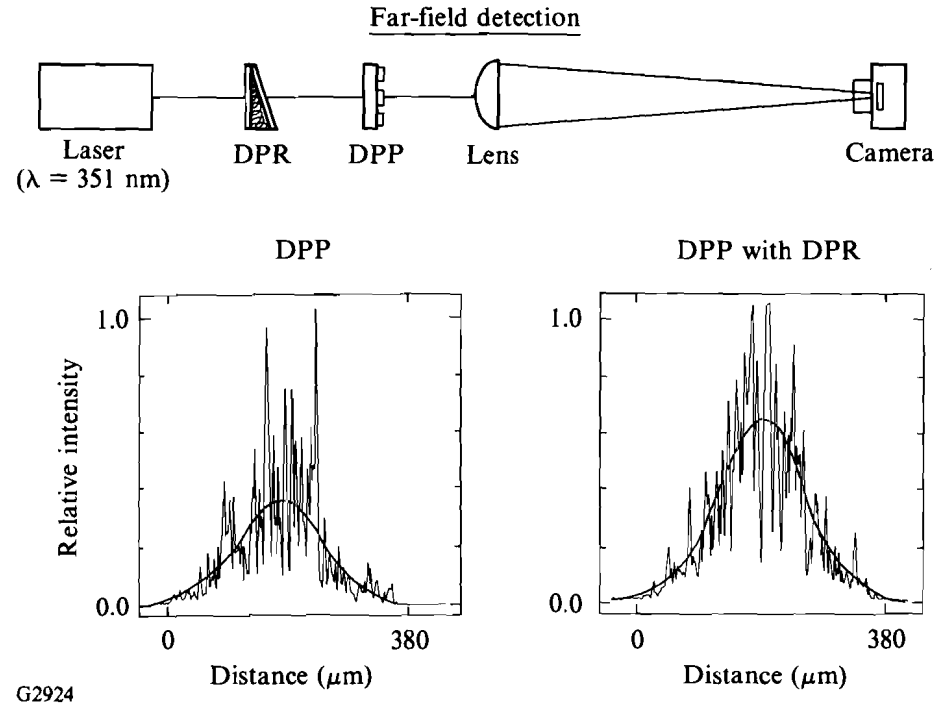


Fig. 45.6
The wedged DPR reduces the speckle intensity modulation in the far field of a DPP. The far-field detection system records the far-field image of the light transmitted through the DPP and DPR. The profile at the left shows an intensity cross section from the DPP pattern. The profile at the right shows an intensity cross section from the combination of a DPP and a DPR. The speckle modulation is reduced by more than $\sqrt{2}$. This is seen by observing that the ratio of peak intensity to average intensity decreases with a DPR.

Time-integrated, equivalent-target-plane focal spots of the combination of broadband phase conversion and distributed polarization rotation have recently been generated on one beam of the OMEGA laser system. Improvements in light uniformity are difficult to diagnose due to the time-integrated effects of SSD and the results do not fully reflect the time-instantaneous benefit. The case in which the polarization cycling and the color cycling are orthogonal shows improvement in uniformity as compared to the case in which they are both parallel. It has been calculated that, by orienting the polarization cycling orthogonal to the direction of color cycling from SSD, a reduction from 4.0% to 2.8% in the time-integrated nonuniformity can be achieved.

It is anticipated that an additional benefit of polarization segmentation may be realized if the DPR is placed well in advance of the DPP. Beam deflection occurs outside the image plane of the source of angular dispersion, i.e., the diffraction grating. By placing the DPR well in advance of the DPP,

the angular dispersion between the elements would produce a spatial deflection that results in a time-varying polarization that samples the individual elements of the DPP. Therefore, if the polarization cycling frequency is high enough to fully sample different elements on the DPP, then an additional source of beam smoothing is expected to contribute to time-dependent uniformity improvements.

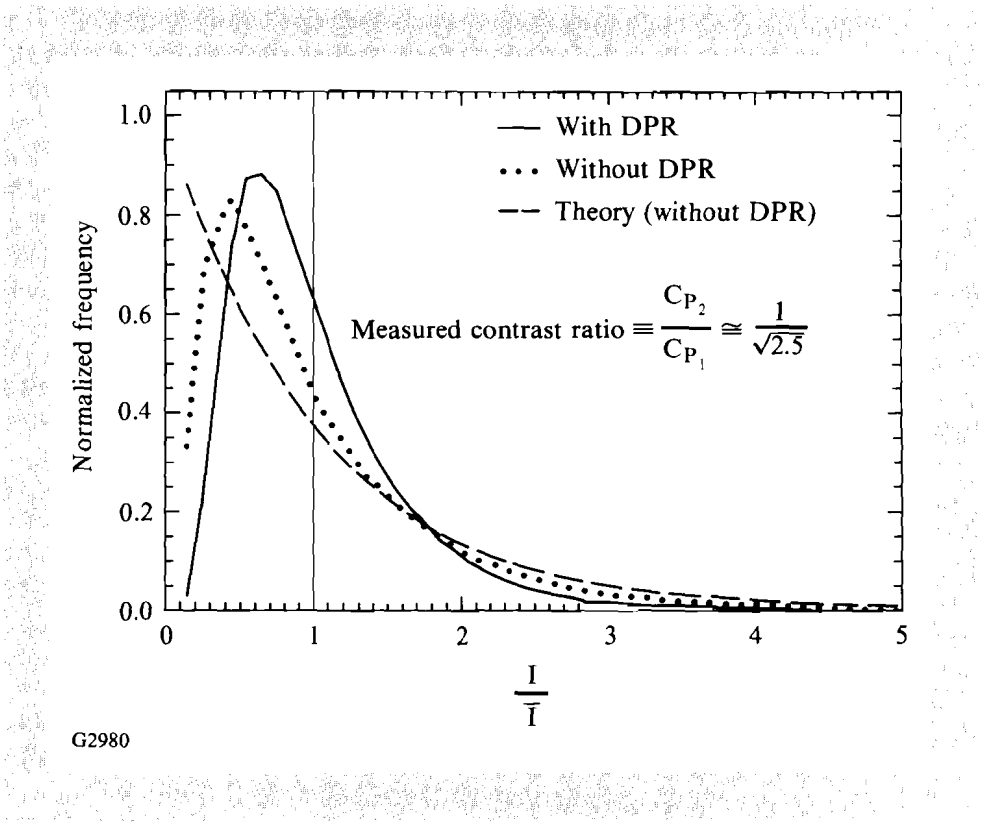


Fig. 45.7
Time-instantaneous decrease in speckle contrast, produced by the DPR, is measured to be greater than $\sqrt{2}$. Assessment of the full benefit of the DPR is currently diagnostic limited, as seen by comparing theoretical and experimental curves for the case with a DPR.

**Summary**

An essential requirement of direct-drive inertial confinement fusion is the uniform irradiation of spherical targets placed in the quasi far field of a laser beam. Phase-conversion technologies continue to provide the OMEGA laser system with substantially improved levels of irradiation uniformity for targets placed close to the far-field plane. Furthermore, the relevant phase-conversion technologies are flexible and inexpensive.

A new phase-conversion technique based on a DPR has been developed to provide smoothing of the laser intensity on target. It has been shown theoretically and experimentally that one-dimensional DPR reduces the contrast of speckle nonuniformities by a factor of $\sqrt{2}$. This technique instantaneously achieves a level of uniformity that current time-domain techniques, such as SSD, require tens of picoseconds to achieve, assuming a time-integrated response from the target. It is expected that a combination of all phase-conversion techniques will provide levels of irradiation uniformity necessary for future direct-drive laser-fusion research.

ACKNOWLEDGMENT

This work was supported by the U.S. Department of Energy Division of Inertial Fusion under agreement No. DE-FC03-85DP40200 and by the Laser Fusion Feasibility Project at the Laboratory for Laser Energetics, which has the following sponsors: Empire State Electric Energy Research Corporation, New York State Energy Research and Development Authority, Ontario Hydro, and the University of Rochester.

REFERENCES

1. S. Skupsky and T. Kessler, *Opt. Commun.* **70**, 123 (1989).
2. R. H. Lehmberg, A. J. Schmitt, and S. E. Bodner, *J. Appl. Phys.* **62**, 2680 (1987).
3. C. Strangio and A. Caruso, *Laser and Particle Beams* **8**, 135 (1990).
4. X. Deng *et al.*, *Appl. Opt.* **25**, 377 (1986).
5. Y. Kato *et al.*, *Phys. Rev. Lett.* **53**, 1057 (1984).
6. LLE Review **33**, 1 (1987).
7. T. Kessler, W. Castle, N. Sampat, S. Skupsky, D. Smith, and S. Swales, in *Proceedings of Conference on Lasers and Electro-Optics*, Optical Society of America, Anaheim, CA, 25–29 April 1988.
8. S. Skupsky, R. W. Short, T. Kessler, R. S. Craxton, S. Letzring, and J. M. Soures, *J. Appl. Phys.* **66**, 3456 (1989).
9. LLE Review **37**, 40 (1988).
10. T. Gunderman, J.-C. Lee, T. J. Kessler, S. D. Jacobs, D. J. Smith, and S. Skupsky, in *Proceedings of Conference on Lasers and Electro-Optics*, Optical Society of America, Anaheim, CA, 21–25 May 1990.
11. "Laser Speckle and Related Phenomena," in *Topics in Applied Physics*, edited by J. C. Dainty (Springer-Verlag, Berlin, Heidelberg, New York, 1975), Vol. 9, Chap. 2.
12. S. D. Jacobs, K. A. Cerqua, K. L. Marshall, A. Schmid, M. J. Guardalben, and K. J. Skerrett, *J. Opt. Soc. Am. B*, **5**, 1962 (1988).
13. S. Papernov, K. Marshall, M. Guardalben, A. Schmid, and S. D. Jacobs, *Liq. Cryst.* **9**, 71 (1991).

## 1.B Hydrodynamic Simulation of Non-LTE Atomic Physics of High-Density Implosions of Argon-Filled, Polymer-Shell Targets

Implosions of argon-filled, plastic-shell targets provide a source for studying the x-ray emission from matter at high temperatures and densities.[1] X-ray line emission itself can be used to diagnose the core conditions in inertial confinement fusion (ICF) targets. Comparison of the core conditions with hydrodynamic simulations can then provide information on target perfor-

mance, especially on the effect of laser-illumination nonuniformity. Two series of experiments were carried out at the Laboratory for Laser Energetics (LLE), in which Ar-filled plastic microballoons were imploded using the 24-beam UV OMEGA laser system.[1,2] The two series had different target radii, fill pressures, and laser conditions. The x-ray emission, measured with both time-integrated and time-resolved spectrographs, showed both emission line broadening and absorption-line features. Analysis of the x-ray line emission from the first series of experiments indicated that core electron densities reached $10^{25}$ cm$^{-3}$ with peak electron temperatures about 1 keV[1] and that a density and temperature gradient existed in the core during the time of emission.[2]

In the following sections we describe the results of the experiments and the corresponding simulations with the hydrodynamic code *LILAC*. In particular, we show from the results of the simulations that the density-broadened lines are emitted during shock convergence to the target center and that the absorption features occur as the shock travels outward after reflection at the target center. This implies that the line emission and the absorption features from the argon core do not measure the peak densities reached at stagnation. Simulations predict a density and temperature gradient in the absorbing region with magnitudes similar to those measured in the experiment. Also, the timing of the occurrence of the emission and absorption spectral features in the simulations agrees well with experimental observations.

**First Series of Experiments**

In the first series of experiments,[1] 420-μm diameter, Ar-filled plastic microballoons with 6-μm shell thickness were imploded using the 24-beam UV ($\lambda = 0.351$ μm) OMEGA laser system. The 680-ps (FWHM) Gaussian pulses provided 1700 J of incident energy. The targets were filled with 10 atm of Ar and were coated with a 0.05-μm layer of Al as a retention barrier for Ar and to prevent the shinethrough of the laser light early in the pulse. It is assumed that argon gas remained diffused into the plastic after the filling process. Improved illumination uniformity was achieved through the use of distributed phase plates (DPP's). The diagnostics included time-resolved x-ray line spectroscopy using SPEAXS[3] and time-integrated x-ray spectroscopy. The time-resolved line-emission spectra, analyzed in Ref. 1, showed that the He-like satellites ($2l2l'$-$1s2l$) of the Lyman-alpha ($L_\alpha$) transition of $Ar^{+17}$ (1s–2p) and the resonant transition merged into a single emission feature because of broadening. Electron densities were obtained by comparing the measured line shapes with Stark-broadened line profiles computed from a multielectron line-profile code.[4] The density and temperature results from that analysis for shot 15772 are shown in Table 45.I.

More recently, the absorption line profiles for the $n = 1$ to $n = 2$ inner-shell transitions present in the time-resolved spectrum for shot 15772 have also been analyzed.[2] Line-outs from this spectrum at different times during the appearance of the absorption feature are shown in Fig. 45.8. The absorption lines for B-, Be-, and Li-like Ar are seen on the low-energy side of the $He_\alpha$ line. The absorption array appears about 50 ps after the broadened

Table 45.I: Density and temperature results from the analysis of data in Ref. (1). Time is measured with respect to the peak of the laser pulse ($1 \times 10^{24}$ cm$^{-3}$ ≈ 4 g/cm$^{-3}$).

| Time Interval (ps) | Electron Density ($10^{24}$ cm$^{-3}$) | Temperature (eV) |
|---|---|---|
| 312–375 | 3–6 | 600–900 |
| 348–405 | 5–7 | 600–800 |
| 375–427 | 6–8 | 500–800 |

TC2913

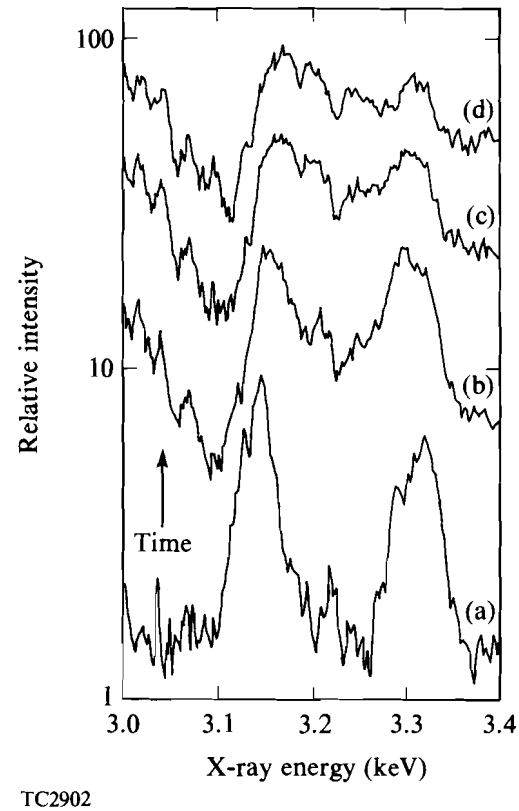


TC2902

Fig. 45.8
Time-resolved x-ray spectrum for shot 15772 in the first series of experiments. These lineouts have been shifted vertically by arbitrary amounts for clarity.

$L_\alpha$ and He-like satellites and is still observed well after the emission lines have merged into the continuum. Stark-broadened absorption profiles, computed from an extended version of the multielectron line-profile code in Ref. 4,[5] were compared to the experimental spectrum for each absorption line using a simple model of attenuation through a uniform absorption layer,

$$I(\nu) = I_0(\nu)\exp(-\tau_\nu),$$

$$\tau_\nu = \frac{\pi e^2}{mc} f\phi(\nu) N_g \ell,$$

where $I_0(\nu)$ is the incident intensity, $I(\nu)$ is the attenuated intensity, $\tau_\nu$ is the optical thickness at frequency $\nu$, $f$ is the average oscillator strength of the 1s–2p absorption transitions of each absorbing ion, $\phi(\nu)$ is the absorption profile, $N_g$ is the absorbing ion density, and $l$ is the path length. The comparison with the experimental spectrum is done in the log (intensity) versus energy plot, and the continuum level is estimated over a broad energy range.

The analysis was carried out for the two line-outs (c) and (d) in Fig. 45.8. For line-out (c), the best fit to the overall absorption features was obtained by using electron densities $n_e = 2 \times 10^{24}$ cm$^{-3}$ for the B-like Ar and $n_e = 1 \times 10^{25}$ cm$^{-3}$ for the Be- and Li-like Ar. Changing the electron temperature from 200 eV to 600 eV did not produce significant differences in the shape of the line profile. The analysis of the absorption feature of line-out (d) yielded similar results: $n_e$ in the range $1 \times 10^{24}$ cm$^{-3}$ to $2 \times 10^{24}$ cm$^{-3}$ fits the B-like Ar transitions, and $n_e = 5 \times 10^{24}$ cm$^{-3}$ fits the Be- and Li-like Ar transitions.

The results of the analysis of the time-resolved spectrum for shot 15772 indicate that densities larger than $5 \times 10^{24}$ cm$^{-3}$ have been achieved in the compressed argon. The fact that two different sets of values for the electron density and temperature were needed to fit the absorption features produced by different ionization states can be attributed to the presence of spatial density and temperature gradients in the argon core. These conclusions will be supported by the results of the simulations.

The simulation of shot 15772 was carried out with the one-dimensional (1-D) hydrodynamic code *LILAC*, a Lagrangian code that includes flux-limited diffusion thermal-electron heat transport, multigroup flux-limited diffusion radiation transport, either local-thermal-equilibrium (LTE) or non-LTE (average-ion model) atomic physics, SESAME equation of state, and ray tracing with a realistic laser-beam profile. The emission spectrum is generated by a postprocessor that includes a detailed-configuration non-LTE model.[6] This postprocessor does not include the presence of satellites and uses *ad hoc* absorption linewidths (trapezoidal line shape with 21-eV FWHM, separated by 22.4 eV). The energies are roughly estimated from the results of an atomic-structure code that provides the spectral distribution and strengths of the individual transitions. A flux-limiter value of 0.06 (sharp cut-

off method) was used in the electron heat transport. This value, used in all the implosion simulations carried out at LLE, provides good agreement with both the measured absorption fraction and the shell-implosion velocity. In these simulations, it was assumed that the density of the argon dissolved in the plastic shell was equal to that in the fill.

The observed occurrence of broad line emission followed by the appearance of absorption lines can be explained by looking at the shock dynamics in the argon fill during the implosion. In gas-filled target implosions, the gas is heated by a shock wave produced by the inward motion of the shell. The shock wave converges to the target center where it is reflected back toward the imploding shell. Each passage of the shock results in higher densities and temperatures. Conditions in the Ar and the simulated spectrum when the shock is reflected at the center of the target are shown in Fig. 45.9. At the center of the target, the shock-heated Ar has reached electron temperatures in excess of 1 keV and electron densities of $3 \times 10^{24}$ cm$^{-3}$. The outer part of the core is colder and less dense than the central part. The simulated spectrum shows both the early absorption features and the Ar $L_\alpha$ emission, which is composed of a strong narrow part emitted by the argon present in the shell and heated by the laser, and a weaker broad base emitted by the dense argon in the core. The narrow part of the line is not observed experimentally at this time (see Fig. 45.8) but can be seen earlier, before the onset of emission from the core. This may be because the density of the argon diffused in the plastic may be much lower than expected. The width of the $L_\alpha$ line in Fig. 45.9 cannot be directly compared with that in the experiment because the

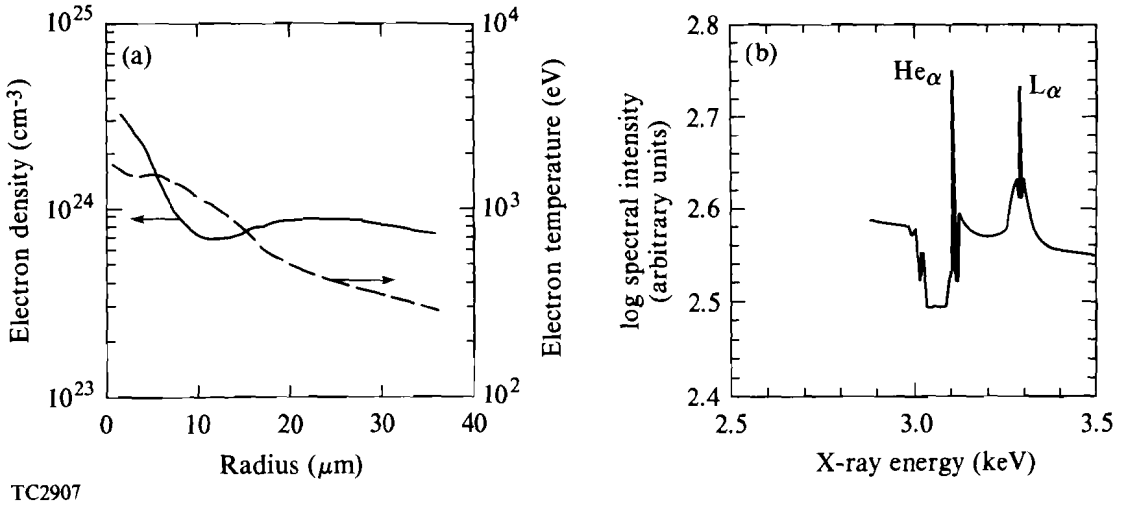


Fig. 45.9
(a) Electron density (solid line) and temperature profiles (dashed line), and (b) simulated spectrum, showing the broadened $He_\alpha$ line for shot 15772. The time is 380 ps, with respect to the peak of the pulse, when the shock is reflected at the target center.

postprocessor does not include satellite emission. The conditions in the emitting region of the Ar compare reasonably well with the measured electron densities and temperatures listed in Table 45.I. As in the experiment, the computed electron density increases with time while the temperature drops slightly because of radiative cooling. The observed temperatures are lower than the computed values probably because the experimental implosion is not perfectly one-dimensional.

The conditions in the Ar core later in time are shown in Fig. 45.10(a), when the shock, after reflection at the target center, is almost halfway back across the core on its way to the plastic shell (at the right edge of the graph). At this time, the electron temperature has dropped to 1 keV, but the electron density has reached $3 \times 10^{25}$ cm$^{-3}$ behind the shock. Under these extreme conditions the central region of the Ar core will emit mostly a continuum spectrum. As this emission travels outward, it passes through the cooler and less dense outer region of the core, where it is absorbed by $n = 1$ to $n = 2$ inner-shell transitions. Three absorption lines, Li-, B-, and Be-like, are observed in the spectrum computed by the postprocessor and shown in Fig. 45.10(b). These are the same absorption lines that are observed experimentally in trace (b) and (c) of Fig. 45.8. Since the line-absorption model in the postprocessor does not include accurate, realistic line profiles that are density dependent, the comparison between the experiment and simulation set of absorption lines should not be regarded as quantitative.

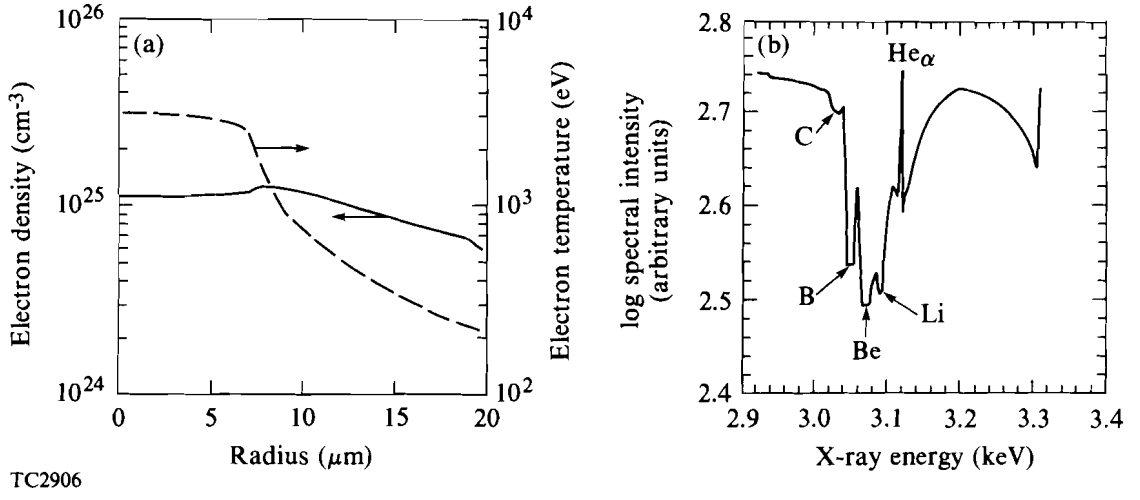


Fig. 45.10
(a) Electron density (solid line) and temperature profiles (dashed line), and (b) simulated spectrum, showing the absorption lines for shot 15772. The time is 450 ps, with respect to the peak of the pulse, when the shock has reflected about halfway to the plastic shell. The absorption lines range from Li-like to C-like.

Although detailed comparison of the line shapes is not available at this time, we can still compare the simulation results with the experimental results in terms of spatial gradients and ionization-state populations. The density and temperature profiles in Fig. 45.10(a) do show both a density and a temperature gradient in the absorbing region, as was suggested by the

analysis of the experimental absorption-line shapes. The ionic population fractions in the Ar core obtained from the postprocessor at the same time as for Fig. 45.10 are shown in Fig. 45.11 as a function of the radius. The Li-like population is relatively constant throughout the core, whereas the B-like population has a minimum where the shock is located. Thus, we would expect that the absorption by the Li-like transition would be dominated by the higher electron density near the core center (5 to $10 \times 10^{24}$ cm$^{-3}$), while the absorption by the B-like transition should be more representative of the lower electron densities near the outer region of the core (2 to $3 \times 10^{24}$ cm$^{-3}$). This is in quantitative agreement with the results of the analysis of the observed spectra, which indicate electron densities of $5 \times 10^{24}$ cm$^{-3}$ for the Li- and Be-like transitions, and 1 to $2 \times 10^{24}$ cm$^{-3}$ for the B-like transitions. There is also a good agreement as to the time at which the absorption features are observed: the trace for spectrum (b) of Fig. 45.8 was averaged over the time interval 400 to 455 ps after the peak of the pulse; the simulation conditions shown in Figs. 45.10 and 45.11 were taken at time 450 ps. The conditions for observing the absorption lines persist until the shock nears the edge of the Ar core. At this time, the core is a very dense sphere of hot Ar at electron densities near or exceeding $1 \times 10^{25}$ cm$^{-3}$ and at temperatures slightly lower than 1 keV, and no structure, except for the emission from the argon in the shell, should be observed in the spectrum.

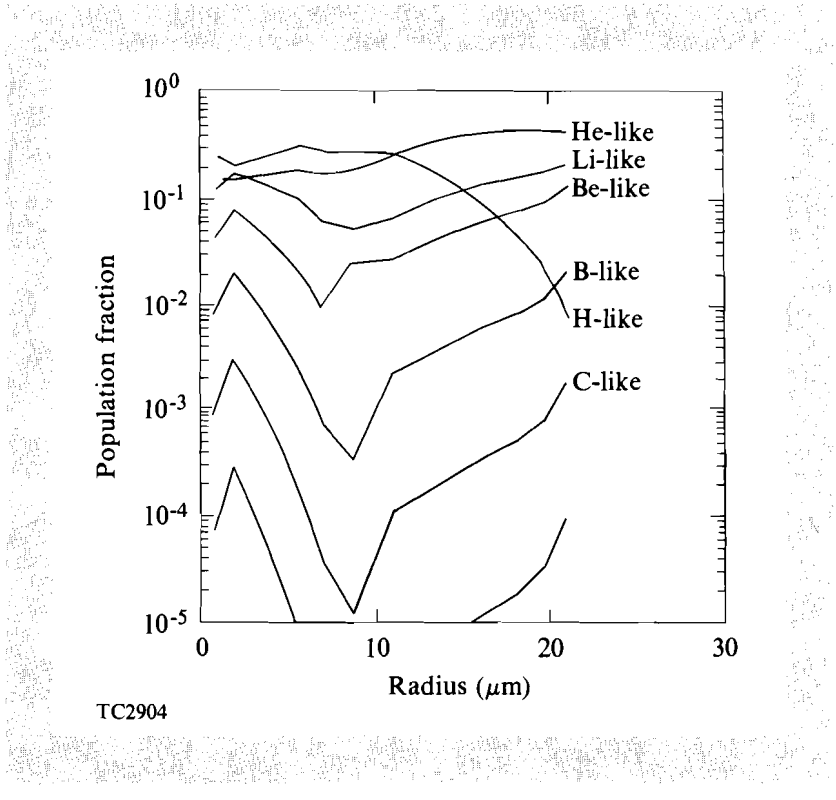


Fig. 45.11
Population fractions for the $n = 1$ to $n = 2$ inner-shell transitions for the conditions in Fig. 45.10.

The distribution of the population fractions shown in Fig. 45.11 as a function of the radius can be explained as follows. When the shock is being reflected at the center of the core, the Ar core consists mainly of an electron-temperature gradient ranging from 200 eV near the outer edge to 1000 eV near the center of the core and of a slowly rising electron density above $1 \times 10^{24}$ cm$^{-3}$. (This condition occurs at a slightly later time than that of Fig. 45.9.) The increase in temperature across the core results in a slowly increasing population fraction for the H-like ionization state combined with decreasing populations for the lower ionization states. As the reflected shock traverses this plasma, the increase in electron temperature leads to an increase in ionization. Behind the shock, the electron temperature decreases slightly because of radiation losses, causing the ionization to decrease. The increase in ionization by the shock explains the drop in the population fraction of the lower ionization states.

**Second Series of Experiments**

In the second series of experiments, Ar-filled microballoons with diameters of 250 μm and plastic thicknesses of 6, 8, 10, and 12 μm were imploded with 600-ps (FWHM), 1200-J Gaussian pulses. The targets were filled with 20 atm of Ar and coated with 0.05 μm of Al. The 24 OMEGA beams included smoothing by spectral dispersion (SSD)[7] at a frequency of 8.45 GHz with a bandwidth $\Delta\lambda/\lambda = 2.7 \times 10^{-4}$. Only the time-integrated spectra, shown in Fig. 45.12, were available for analysis because the time-resolved spectra were too weak to be analyzed in the same manner as the

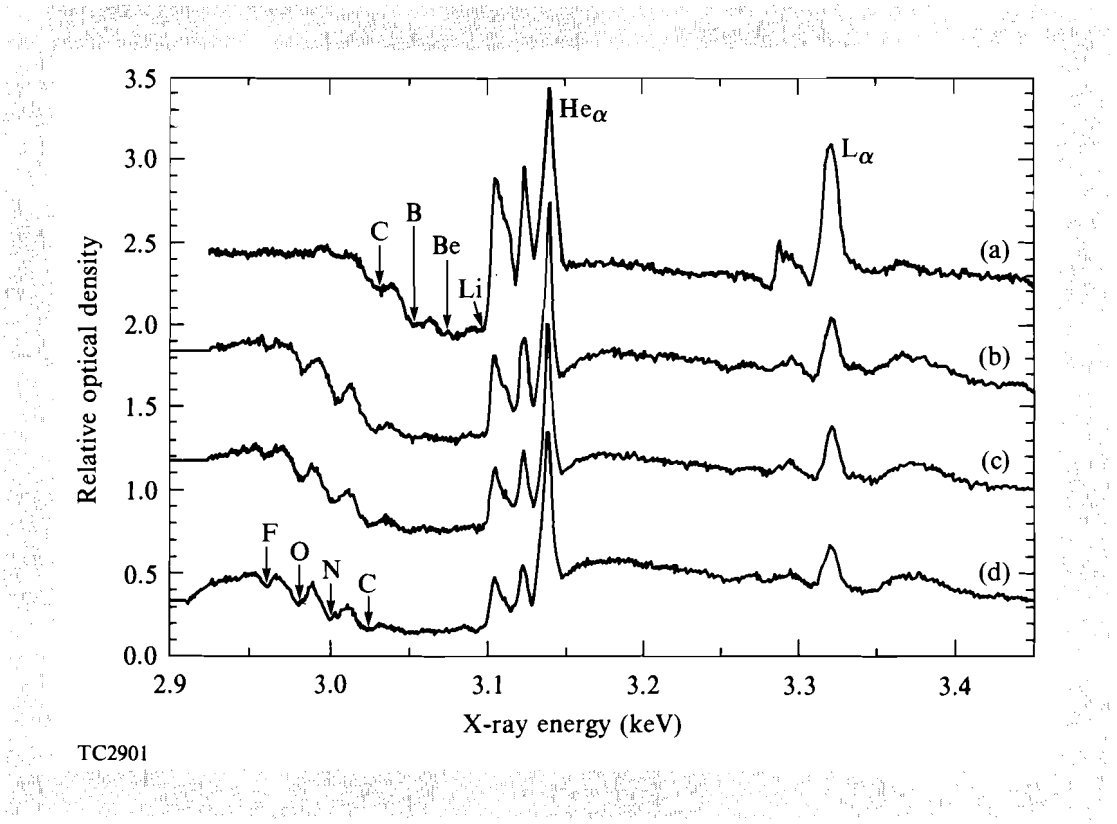


Fig. 45.12
Time-integrated x-ray spectra for targets with increasing wall thickness in the second series of experiments. The wall thicknesses are (a) 6 μm, (b) 8 μm, (c) 10 μm, and (d) 12 μm.

time-resolved spectrum for shot 15772. No detailed analysis was carried out for the absorption features visible on the low-energy side of the $He_\alpha$ resonance line. The spectra show that the lowest ionization state observed in each spectrum decreases as the plastic thickness increases: from C-like for the 6-μm-thick target to F-like for the 12-μm-thick target. This observation implies that the absorbing region of the Ar core is colder in the thick-walled target implosions than in the thin-walled target implosions. Unlike the first series of experiments, the broad emission feature consisting of the density-broadened He-like satellites and the $L_\alpha$ resonance line was not observed. Preliminary results from simulations indicate that the emission level of the Stark-broadened Ar $L_\alpha$ in the second series of experiments should be lower than that in the first series. Thus the time-integrated $L_\alpha$ emission is probably dominated by the narrow emission from the Ar dissolved into the plastic and directly heated by the laser in the corona.

In this series of experiments, simulations were carried out for only two plastic thicknesses: 6 μm and 12 μm. The electron temperatures and densities from the simulation for the 6-μm case are similar to the results of the simulations of shot 15772. (The reduction in target diameter, and hence in the mass, was compensated for by a reduction in the incident laser energy and absorption fraction.) An exception is that, at the time of shock reflection at the center, the broadened part of the Ar $L_\alpha$ emission is weaker in the second series than in the first series of experiments. This is probably because there are fewer emitters in the second series: the number of Ar ions in the targets of the second series is about half that in the first series. At the time the shock has returned halfway through the core, the predicted spectrum for the 12-μm-thick target in Fig. 45.13(b) shows absorption lines from the Li-like to the N-like states. Its lowest ionization state (N-like) is higher than that in the experimental spectrum (O-like and F-like). This implies that the absorbing outer region of the Ar core is cooler than predicted. The appearance of

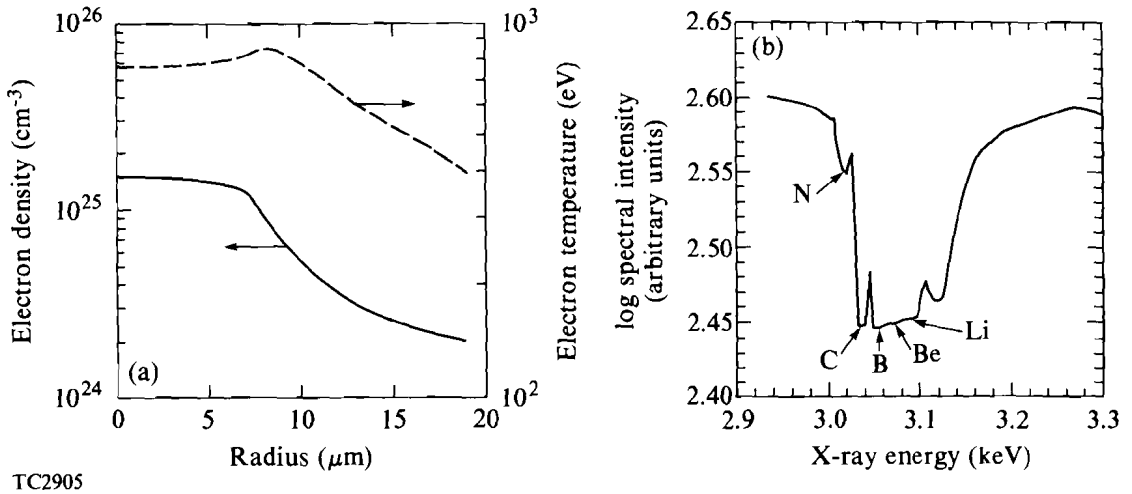


Fig. 45.13
(a) Electron density (solid line) and temperature profiles (dashed line), and (b) simulated spectrum, showing the absorption lines for the 12-μm case in Fig. 45.12. The time is 515 ps with respect to the peak of the pulse. The absorption lines range from Li-like to N-like.

absorption lines from lower ionization states than in the 6-μm case (and also in shot 15772) is caused by lower electron temperatures in the absorbing region rather than by a larger $\rho\Delta R$ in that region. This is seen in Fig. 45.13(b), which shows conditions in the Ar core: the electron temperature is about 400 to 500 eV compared to 600 to 700 eV for the 6-μm case (Fig. 45.10), while the core radii are about the same and the electron density is lower for the 12-μm case than for the 6-μm case. Both the peak electron temperature and the peak electron and ion densities are lower in the 12-μm case than in the 6-μm case: the peak electron density reached by the 12-μm-thick target is about half the density obtained by the 6-μm-thick target. The 12-μm target has a lower performance than the 6-μm target because of its larger mass and, therefore, reduced implosion velocity.

We can estimate the lower bounds of the areal density required to observe an absorption line. The optical depth of an absorption line depends on the magnitude of the integrated absorption areal ion density $n_i(r)\Delta R$ for each ionization state, where $n_i$ is the ion density and $\Delta R$ is the incremental path length at that density. In the time-resolved spectrum for shot 15772 (Fig. 45.10), the C-like line is barely visible. In Fig. 45.11 the C-like population fraction reaches $10^{-3}$ over a short distance leading to an areal ion density of about $2 \times 10^{-7}\ n_i\ \text{cm}^{-2}$, or about $4 \times 10^{17}\ \text{cm}^{-2}$. In the second series of experiments, the N-like absorption line is slightly deeper than the C-like line in the first series. In Fig. 45.14 the population fraction for the N-like state is about $2 \times 10^{-3}$ over 2 μm yielding an areal ion density of about $8 \times 10^{17}\text{cm}^{-2}$. The value of the areal ion density will vary over time as the

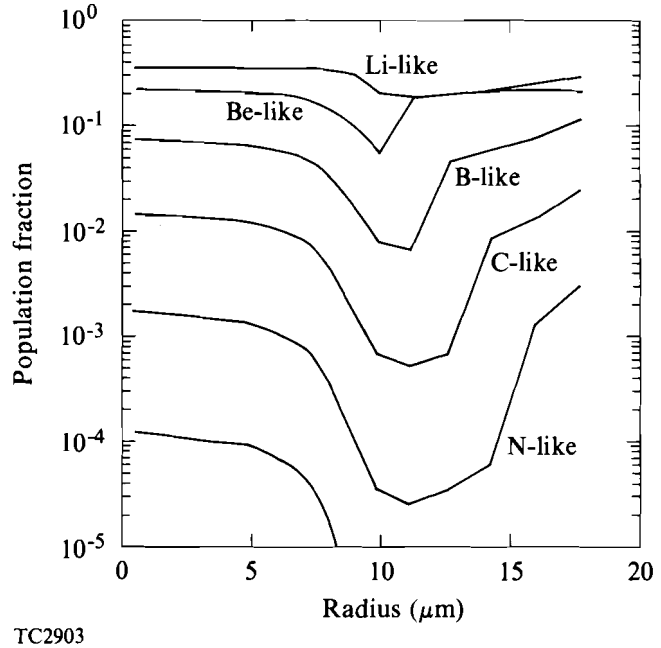


Fig. 45.14
Population fractions for the $n = 1$ to $n = 2$ inner-shell transitions for the conditions in Fig. 45.13.

shock travels toward the edge of the Ar core. While a quantitative analysis of the temporal variation of the areal ion density is beyond the scope of this article, we can estimate that the absorption line analysis can observe areal ion densities in Ar of about $4 \times 10^{17}$ cm$^{-2}$ for each ionization state. For the ionization levels computed in the simulations, this is equivalent to about $2 \times 10^{-3}$ g/cm$^{-2}$.

## Conclusions

Two series of experiments have been analyzed in which argon-filled plastic shells were imploded to generate high-density and high-temperature conditions in the Ar core. Time-resolved and time-integrated spectra showed density-broadened emission and absorption lines. The emission lines were observed to emit about 50 ps before the absorption lines. Analysis of the emission lines from 6-μm-thick targets indicates that they originated from a plasma with electron density between $3 \times 10^{24}$ cm$^{-3}$ and $8 \times 10^{24}$ cm$^{-3}$ and temperatures ranging from 500 to 800 eV. Absorption lines from Li-, B-, and Be-like configurations were observed and their shape fitted to theoretical line shapes. The result of this analysis implies the presence of a density gradient between 1 to $2 \times 10^{24}$ cm$^{-3}$ and $5 \times 10^{24}$ cm$^{-3}$ with temperatures between 200 and 600 eV. In implosions with thicker plastic shells, the emission lines were found to be weaker and not as broadened, and absorption lines were observed for ionization states up to F-like Ar.

Simulations carried out with the 1-D hydrodynamic code *LILAC* indicate that the density-broadened lines are emitted when the shock, formed in the Ar core by the imploding CH shell, reaches the center of the target. The absorption lines are observed at a slightly later time, when the shock has reflected from the target center and is traveling back toward the shell. During this time, the central part of the Ar core emits continuum radiation caused by the high electron density (>$10^{25}$ cm$^{-3}$), which is absorbed in the cooler and less-dense outer region of the core. The simulations predict an electron density and temperature gradient in the absorbing region with magnitudes similar to those measured. Also, the timing of the observation of the emission and absorption spectral features agrees roughly with the code predictions. Finally, for the 12-μm-thick target, the lowest ionization state for the absorption lines is predicted to be N-like, whereas the F-like state was observed experimentally. This indicates that the electron temperature in the absorbing outer region of the core must have been lower than those predicted.

These are the first reported experiments in which the core of a target is characterized in such detail, especially after shock reflection from the center. This indicates that the target must have survived the effects of laser illumination nonuniformity and remained reasonably intact during the implosion. There are some indications, however, that the implosion was not perfectly one-dimensional: the electron temperature obtained from the analysis of the emission line is lower by a factor of 2 than the predicted temperatures, thus implying that the shock convergence was not one-dimensional. The disagreement on the lowest observable ionization state in the absorption array of the 12-μm case could be interpreted as the result of mixing of the cold

plastic-shell materials into the hotter Ar of the absorbing region. This effect was not observed in shot 15772 (6-μm shell) because the ionization state is more sensitive to small variations in electron temperature at the low ionization states than at the high ionization states.

One conclusion from the simulations is that line emission and absorption from the Ar core do not measure the peak densities attained at stagnation. Broadened emission lines can only be observed for the electron densities present at the time when the shock reaches the target center; at higher densities ($>10^{25}$ $cm^{-3}$) the lines merge into the continuum. The absorption lines can only furnish information about the plasma in the region between the reflected shock and the shell, whereas the peak density actually occurs behind the shock in the central part of the core. Despite these restrictions, we have shown that imploding, Ar-filled plastic targets can provide the conditions required to study the radiative properties of matter at high temperatures (about 1 keV) and high densities (about $10^{25}$ $cm^{-3}$).

## ACKNOWLEDGMENT

This work was supported by the U.S. Department of Energy Division of Inertial Fusion under agreement No. DE-FC03-85DP40200 and by the Laser Fusion Feasibility Project at the Laboratory for Laser Energetics, which has the following sponsors: Empire State Electric Energy Research Corporation, New York State Energy Research and Development Authority, Ontario Hydro, and the University of Rochester.

## REFERENCES

1. C. F. Hooper, Jr., D. P. Kilcrease, R. C. Mancini, L. A. Woltz, D. K. Bradley, P. A. Jaanimagi, and M. C. Richardson, *Phys. Rev. Lett.* **63,** 267 (1989).
2. R. C. Mancini, C. F. Hooper, Jr., J. Delettrez, R. Epstein, D. K. Bradley, P. A. Jaanimagi, and M. C. Richardson, in *Proceedings of the International Workshop on Radiative Properties of Hot Dense Matter,* Sarasota, FL (to be published).
3. B. L. Henke and P. A. Jaanimagi, *Rev. Sci. Instrum.* **56**, 1537 (1985).
4. L. A. Woltz and C. F. Hooper, Jr., *J. Phys. A* **21**, 4766 (1988).
5. R. C. Mancini, D. P. Kilcrease, L. A. Woltz, and C. F. Hooper, Jr., *Comp. Phys. Comm.* (to be published).
6. R. Epstein, *Phys. Fluids B* **1**, 214 (1989).
7. S. Skupsky, R. W. Short, T. Kessler, R. S. Craxton, S. Letzring, and J. M. Soures, *J. Appl. Phys.* **66**, 3456 (1989).

# 1.C Satellite Absorption Lines and the Temperature Dependence of X-Ray Absorption Features in High-Temperature Plasmas

In absorption spectroscopy, absorption features impressed on the spectrum of a continuum background source are interpreted in terms of conditions in an absorbing foreground medium. If the opacity per ion for a particular transition beginning from some initial state is known, then the areal density (i.e., the path integral of the density along the path of the continuum propagation) of ions in that state within the absorbing medium can be inferred from the attenuation of the background continuum due to that transition.[1,2] If the relative abundance of ion species can be determined in this way, then temperature can also be inferred from the observed state of ionization, which can be modeled in terms of temperature and density.[2]

In spectra from inertial confinement fusion experiments, the absorption features of interest are unresolved bands of lines from certain ion species, rather than individual lines. The ground configuration and certain low-lying excited configurations of a given ion species each contribute an array of absorption lines to the absorption band of that species. The purpose of this article is to consider the contribution of the excited configurations to the total average absorption strengths of these bands. These excited configurations have not been mentioned explicitly in the earliest published reports on absorption spectroscopy in implosion experiments.[1,2] Among these, the exemplary quantitative analysis by Hauer *et al.*[2] of absorption arrays from an imploded target does not include them. The importance of excited configurations was first considered at the time of this early work,[3] and later by direct comparison of a more complete model[4] with Hauer *et al.*[2] States in the excited configurations have been included in recent detailed models,[4–7] but a general description of the effects of the excited configurations on absorption spectra has yet to be provided. This article aims to provide such a description for two reasons: (1) interesting aspects of these effects can be understood in general terms, and (2) the added insight puts important earlier work into proper perspective.

Ions in the low-lying excited configurations are abundant, and their populations vary widely over the range of temperature found to be typical of conditions in compressed targets. In fact, most of the absorption seen in absorption bands can be due to satellite transitions originating from states in excited configurations. As a result, the total absorption strength per ion of a given species, within a given band, due to all configurations, is temperature dependent and cannot be treated as a constant, as if it were effectively an intrinsic atomic property. Quantitative interpretations of absorption spectra must take this into account.[3]

Laser-driven inertial confinement experiments, particularly the kind where absorption spectroscopy can be used,[1,2] have been described thoroughly elsewhere.[8] In general, they use a small, hollow, spherical target, a

few hundred to several hundred microns in diameter, which is uniformly illuminated with intense laser beams at a total power level of the order of a terawatt for a length of time of the order of a nanosecond. The target, a shell composed mainly of glass, plastic, or both, is either filled with gas or evacuated. Energy absorbed from the laser illumination vaporizes the exterior of the target, which ablates away at high velocity so that the remainder of the target implodes under the force of the reaction to the acceleration of the ablated plasma. Eventually, the imploding shell is stopped by the pressure of the enclosed gas or by the impact when the interior surface of the target meets itself at the center of the implosion. This compression at the center of the target creates conditions of high density and temperature that produce a burst of continuum radiation at or near the time of peak compression. To reach the spectrograph, this radiation passes through what is left of the imploded shell of the target. This unablated remnant of the original target shell is heated during the implosion by compression and a combination of thermal conduction and radiative transport of energy from the outer region of the target that is directly heated by the laser irradiation. The shell remnant can be expected to reach the very broad temperature range where light elements in the neighborhood of chlorine (e.g., silicon through calcium) would be ionized to fluorine-like through helium-like states, the L-shell species.[2] This temperature can vary a great deal, depending on the nature of the experiment, and is typically of the order of a few hundred electron volts, which is an order of magnitude less than the temperatures in the ablation region and in the compressed core. Since these ions have partially vacant L shells, absorption can occur via inner-shell transitions of the kind 1s–2p, which imprints absorption lines on the passing background continuum. These absorbing elements either occur naturally in the shell material itself, e.g., silicon in glass,[1] or they can be introduced as an additive or deposited as a thin concentric layer inside the shell.[2]

At typical shell temperatures, 2s–2p transitions are readily excited by electron collisions, and the excited configurations are heavily populated. The statistical weights of some excited configurations are much larger than those of the respective ground configurations, which can make them even more abundant than the ground configurations, under some conditions. The average 1s–2p absorption strengths of excited configurations are lower than those of ground configurations because the prior 2s–2p excitation has reduced the vacancy of the 2p subshell. The change in 2p vacancy is the primary factor affecting differences in the average 1s–2p absorption strengths among the low-lying configurations of a given species.[3] This reduction is compounded when both 2s electrons are excited, which also occurs readily. Excited oxygen-like and fluorine-like configurations that have full 2p subshells have no 1s–2p opacity at all.

The full spread in excitation energy from the ground state through the excited configurations is roughly 100 eV for the L-shell species of chlorine, which is comparable to, if not less than, the expected shell temperatures. Consequently, the relative populations of the configurations of a given species are temperature dependent. This makes the total 1s–2p absorption

strength per ion, averaged over the same L-shell configurations, temperature dependent as well. Within this range of energy, the states within each configuration are grouped closely in energy. For the relevant species of chlorine, they are typically within 20 eV of each other, often much closer. Since this spread in energy is much less than the anticipated temperatures, the populations of the states within each configuration can be treated, with reasonably good accuracy, as if their populations are distributed relative to each other according to their respective statistical weights. In this approximation, the average 1s–2p opacity per ion within each configuration is independent of temperature.

The terminology "unresolved transition array" has been introduced by Bauche *et al.*[9] to describe the array of lines due to the total of all transitions from one given configuration to another. Statistically weighted configuration averages of line strengths and level populations are the basis for their analysis of broad, unresolved features in x-ray spectra of complex ions. The arrays of lines forming the 1s–2p absorption bands are illustrated in Fig. 45.15 for a few different ionization species of chlorine. The arrays due to each

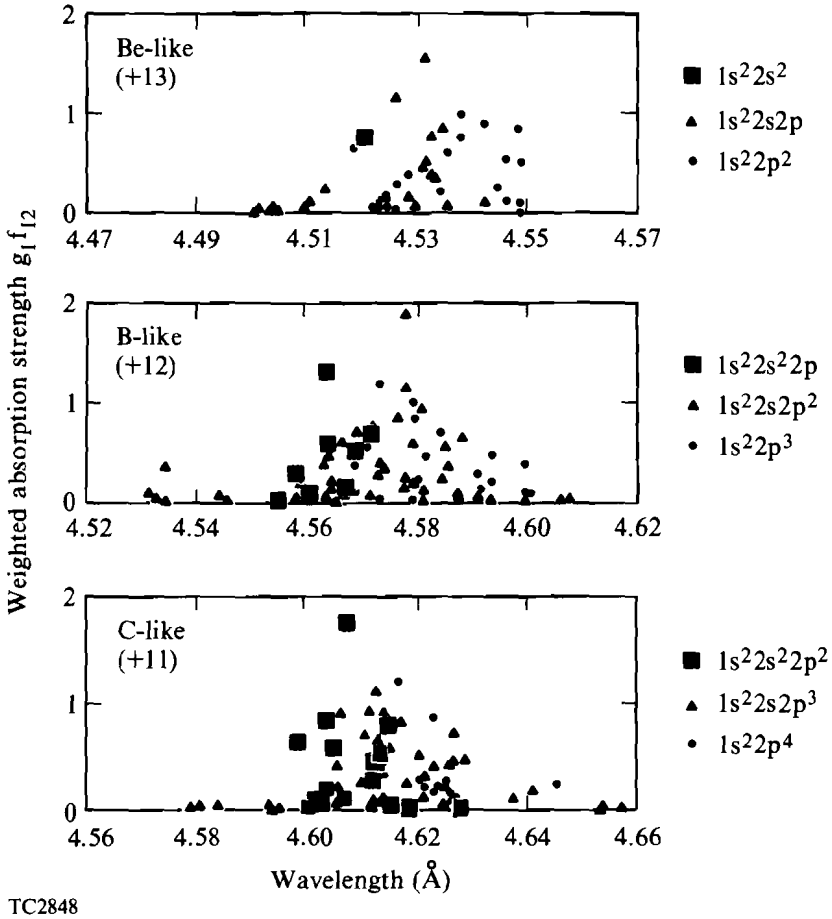


Fig. 45.15
Total statistical-weighted oscillator strengths for all significant (i.e., $g_1 f_{12} > 0.01$) transitions are plotted separately for the beryllium-like, boron-like, and carbon-like ionization species of chlorine. Transitions from the different initial configurations are distinguished. The line arrays from individual configurations are wider than the differences among the average transition energies for each configuration, but the total absorption bands for each species are separate enough to be distinct.

contributing configuration overlap within each band, even though the ranges of energy levels of the different initial configurations do not. Values of the statistically weighted absorption-oscillator strengths $g_1 f_{12}$ for all significant (i.e., $g_1 f_{12} > 0.01$) transitions are plotted at their respective energy. Transitions originating from states in different initial configurations are distinguished by different point symbols. The line arrays for these species are roughly 20 eV in width, which is greater than the differences between the average transition energies for each configuration. The absorption bands for each species are located at energy intervals comparable to their intrinsic width. The shift and broadening of the absorption bands due to temperature-dependent effects on the populations of the initial configurations will be at most only of the order of a few electron volts. Usually, the contribution of excited configuration lines increases the intrinsic widths of the absorption bands only slightly. In the case of the Be-like array, however, the ground configuration has only one allowed 1s–2p transition,[2] so it is specifically the excited configurations that give the total absorption feature the broad appearance of an array of many lines. These results, as well as all other atomic-code results used in this article, were obtained using the relativistic, parameterized potential, multiconfiguration atomic-structure code of Klapisch *et al.*[10]

For the purpose of interpreting an absorption spectrum, it is sufficient to treat each absorption band as a single feature with an effective absorption strength obtained by averaging over all initial configurations, including the excited configurations. The effect of adding the excited configurations to a model of these effective absorption strengths can be expressed as a temperature-dependent correction factor that multiplies the average opacity of the ground configuration. It will be seen that the reduced 2p vacancy of the excited configurations reduces the average opacity of the 1s–2p transitions by as much as about 25% in the high-temperature limit, so estimated areal densities, being inversely proportional to the assumed average opacity, can be low by as much as about 33% if the effect of excited states is not taken into account.

**The Correction Factor**

The different initial configurations of the absorption transitions of chlorine are separated by 2s–2p transition energies less than about 100 eV, and the energies of the fine-structure transitions within each configuration are much less. With temperatures of the order of 100 eV and with electron densities near $10^{22}$ cm$^{-3}$ and above, transitions among these L-shell excited states are almost entirely collisional, so their population ratios are fixed by detailed balance between collisional excitation and its inverse. Consequently, the populations $P_1$ and $P_2$ of any two such states obey the Boltzmann ratio

$$\frac{P_2}{P_1} = \frac{g_2}{g_1} e^{-(E_2 - E_1)/kT} , \tag{1}$$

where the statistical weights of the two states are $g_1$ and $g_2$, respectively, and the respective energies $E_1$ and $E_2$ are to be given in the same units as the

temperature $kT$. At temperatures comparable to the excitation energies, the exponential factor in Eq. (1) is close to unity, and the excited states with large statistical weights can easily be more abundant than the ground state.

The absorption cross section of an individual line is of the form

$$\sigma_i(\nu) = \sigma_i \phi_i(\nu) , \tag{2}$$

where $\phi_i(\nu)$ is the line profile, normalized to unity with respect to frequency $\nu$, and where $\sigma_i$ is the integrated cross section of the transition. The attenuated intensity $I(\nu)$ remaining after the incident background continuum intensity $I_0$ passes through a homogeneous layer of thickness $\Delta r$ of material with a number density $N_I$ of an absorbing species is

$$ln\left(\frac{I_0}{I(\nu)}\right) = N_I \Delta r \frac{\sum_i P_i \sigma_i \phi_i(\nu)}{\sum_i P_i} , \tag{3}$$

where the sum is over all states of the absorbers. The areal density of the absorbing species $N_I \Delta r$ can be obtained from the integrated attenuation and from the total average integrated cross section $\sigma_{tot}$ using

$$\int ln\left(\frac{I_0}{I(\nu)}\right) d\nu = N_I \Delta r \sigma_{tot} , \tag{4a}$$

where

$$\sigma_{tot} = \frac{\sum_i P_i \sigma_i}{\sum_i P_i} . \tag{4b}$$

A more detailed analysis, including radiation transport with detailed descriptions of line profiles, is needed when the attenuation is complete enough to be unmeasurable,[4,6,11] or when Stark broadening becomes significant enough to have diagnostic value.[7] Otherwise the line profiles need not be considered further.[2]

Equation (4b) is evaluated using $P_i$ from Eq. (1). As was discussed in the introduction, one can assume that the states of each initial configuration occur sufficiently close in energy to the average energy of the configuration for this evaluation to be simplified, following the approach of Bauche *et al.*,[9] by grouping terms in the sum by configuration so that each group represents a single transition array, the statistically weighted sum of all transitions from one configuration to another. In this approximation, the same temperature-dependent exponential applies to all states in each configuration, which leaves these populations fixed relative to each other according to their statistical weights. Equation (4b) then becomes

$$\sigma_{\text{tot}} = \frac{\sum_j g_j \sigma_j e^{-(E_j - E_1)/kT}}{\sum_j g_j e^{-(E_j - E_1)/kT}}, \tag{5}$$

where the index $j$ denotes the initial configurations, $1s^2 2s^2 2p^n$ (ground, $j = 1$), $1s^2 2s 2p^{n+1}$, and $1s^2 2p^{n+2}$, or however many of these have no more than five 2p electrons. $E_j$ and $\sigma_j$ are now configuration averages and $g_j$ is the total statistical weight of configuration $j$.

Equation (5) has only one distinct temperature-dependent exponential term for each initial configuration, rather than one term per state, as in Eq. (4b), but these terms do adequately represent the temperature dependence associated with the characteristic excitation energies of each configuration. The effect of this approximation is that all state populations within a configuration change simultaneously as the temperature is varied, rather than in the order of their excitation energy. Since this ordering occurs over small energy differences, compared with anticipated temperatures, errors will also be small, except in the limit where the temperature falls below the energy intervals separating the levels of the ground configuration so that statistical weights alone no longer describe the partition of the ground-configuration populations.

The correct temperature-dependent average cross section can be recovered from the average absorption cross section $\sigma_1$ of the ground configuration by applying the correction factor

$$\frac{\sigma_{\text{tot}}}{\sigma_1} = \frac{\sum_j g_j (\sigma_j / \sigma_i) e^{-(E_j - E_1)/kT}}{\sum_j g_j e^{-(E_j - E_1)/kT}}. \tag{6}$$

The differences among the cross sections of the possible initial configurations are primarily due to differences in the vacancy of the 2p subshell. The 2s–2p excitation does change the distribution of spectator charge in the ion, but, to a very close approximation, the ratio $\sigma_j/\sigma_1$ in Eq. (6) can be replaced by the ratio of the 2p vacancies of the two configurations.

The statistical weights, vacancies, and excitation energies needed to evaluate Eq. (6) for the case of chlorine are given in Table 45.II. The excitation energies are the statistical-weight average energy of all states within the indicated configuration, as obtained using the atomic structure code by Klapisch *et al.*[10] The correction factor given by Eq. (6) is shown plotted in Fig. 45.16 as a function of temperature for all the relevant ionization species of chlorine. The total 1s–2p absorption cross section for a particular ionization species is obtained from the total cross section of the ground configuration alone by applying this correction factor. At lower temperatures, the excited configurations are nearly empty, and there is no

Table 45.II: Average parameters for the configurations of chlorine ions.

| Configuration | Excitation Energy (eV) | 1s–2p Energy (eV) | (Å) | gf | Statistical Weight | 2p Vacancy |
|---|---|---|---|---|---|---|
| Helium-like | | | | | | |
| $1s^2$ | | 2778.0 | 4.463 | 0.882 | 1 | 6 |
| Lithium-like | | | | | | |
| $1s^22s$ | | 2756.0 | 4.499 | 1.559 | 2 | 6 |
| $1s^22p$ | 32.3 | 2753.0 | 4.504 | 3.860 | 6 | 5 |
| Beryllium-like | | | | | | |
| $1s^22s^2$ | | 2737.0 | 4.530 | 0.745 | 1 | 6 |
| $1s^22s2p$ | 32.6 | 2731.0 | 4.540 | 7.594 | 12 | 5 |
| $1s^22p^2$ | 42.6 | 2728.0 | 4.545 | 7.484 | 15 | 4 |
| Boron-like | | | | | | |
| $1s^22s^22p$ | | 2711.0 | 4.574 | 3.657 | 6 | 5 |
| $1s^22s2p^2$ | 39.8 | 2708.0 | 4.579 | 14.705 | 30 | 4 |
| $1s^22p^3$ | 52.3 | 2705.0 | 4.584 | 7.262 | 20 | 3 |
| Carbon-like | | | | | | |
| $1s^22s^22p^2$ | | 2689.0 | 4.611 | 7.090 | 15 | 4 |
| $1s^22s2p^3$ | 49.2 | 2686.0 | 4.616 | 14.230 | 40 | 3 |
| $1s^22p^4$ | 61.4 | 2683.0 | 4.621 | 3.500 | 15 | 2 |
| Nitrogen-like | | | | | | |
| $1s^22s^22p^3$ | | 2669.0 | 4.646 | 6.867 | 20 | 3 |
| $1s^22s2p^4$ | 57.8 | 2666.0 | 4.651 | 6.867 | 30 | 2 |
| $1s^22p^5$ | 69.7 | 2663.0 | 4.656 | 0.676 | 6 | 1 |
| Oxygen-like | | | | | | |
| $1s^22s^22p^4$ | | 2650.0 | 4.679 | 3.288 | 15 | 2 |
| $1s^22s2p^5$ | 65.7 | 2647.0 | 4.684 | 1.317 | 12 | 1 |
| $1s^22p^6$ | 77.3 | | | 0.0 | 1 | 0 |
| Fluorine-like | | | | | | |
| $1s^22s^22p^5$ | | 2632.0 | 4.711 | 0.635 | 6 | 1 |
| $1s^22s2p^6$ | 92.4 | | | 0.0 | 2 | 0 |

TC2910

correction. At higher temperatures, it is interesting that all the species, except helium-like and lithium-like, approach the same limit of 0.75.

**The Screened Hydrogenic Approximation**

In evaluating the correction factor from Eq. (6), the same statistical weights and vacancies apply for the L-shell species of other elements; only

the excitation energies differ. To obtain these excitation energies, average configuration energies from the screened hydrogenic approximation[12–15] are convenient. From comparisons with results from numerical atomic-structure calculations shown below, it can be seen that the screened hydrogenic approximation is adequate.

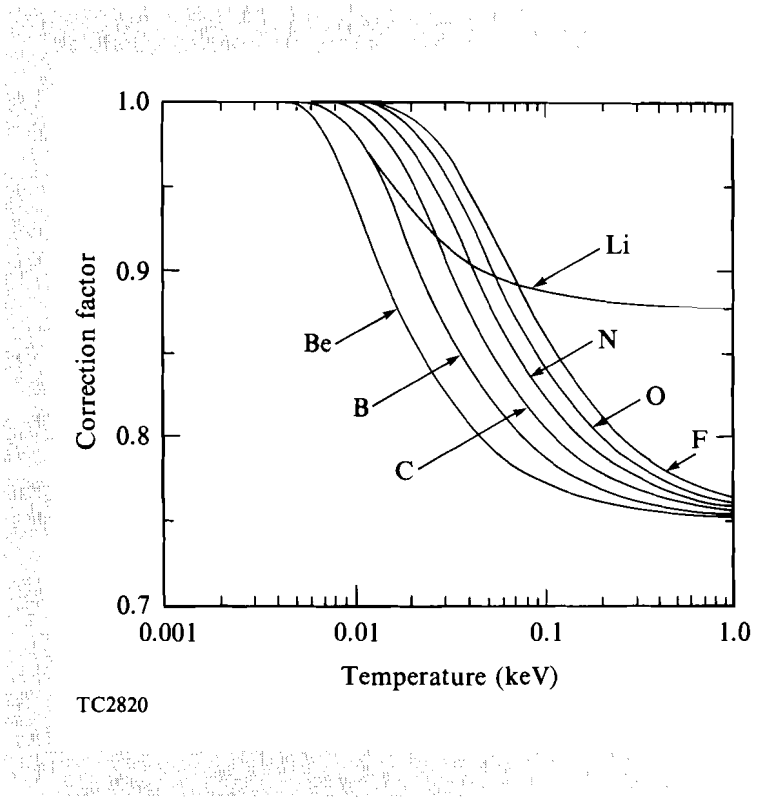


Fig. 45.16
The correction factor given by Eq. (6) is plotted for the relevant ionization species of chlorine. The total 1s–2p absorption cross section for a particular species is obtained from the total cross section of the ground configuration alone by applying the appropriate factor.

In the screened hydrogenic approximation, the energy of any one bound electron is calculated as if it were a single electron bound by a point nucleus whose effective charge is that of the bare nucleus $Z$ minus the effective screening contribution due to the other electrons.[12] The screening of the nuclear charge, as it is seen by an electron in a particular shell, is given by the number of electrons in each shell multiplied by the appropriate respective screening coefficient for each shell.[13] This approach is very convenient for applications where errors of several percent in level energies are not serious.[14,15] These coefficient sets are usually given in terms of the occupation numbers of the principal quantum shells only. Slater's original screening coefficients distinguish between certain subshells, but the $s$ and $p$ subshells are treated as one shell.[12] Mayer has derived two tables of screening coefficients, one in terms of principal quantum shells only, and a shorter table, up to $n = 3$, where the different subshells are distinguished.[13] These are shown in Tables 45.III(a) and 45.III(b), respectively.

The total energy of an ion, in rydbergs, is obtained from the energies $E_n$ and occupation numbers $p_n$ of each principal shell $n$ using the expression

$$E_{\text{ion}}(Ry) = \sum_n p_n E_n \ . \tag{7a}$$

The energy of each shell is given by the hydrogenic expression

$$E_n = -\left(\frac{Q_n}{n}\right)^2 , \tag{7b}$$

where $Q_n$ is the effective nuclear charge seen by the electrons in shell $n$, where $n$ is the principal quantum number of that level.[13] Level $n$ can be either a shell or a subshell. The effective charge, according to the prescription of Mayer, is given by

$$Q_n = Z - \sum_{m \neq n} p_m \sigma_{nm} - p_n \left(1 - \frac{1}{g_n}\right)\sigma_{nn} , \tag{8}$$

where $g_n$ is the capacity of shell $n$ and the screening coefficients $\sigma_{nm}$ specify the effect of the electrons in shell $m$ on the screened charge.[13,16] This prescription applies whether the shells are entire principal shells or individual $n,l$ subshells.[13] The prescription of More is nearly the same, except that the values of the screening coefficients are slightly different, and the effective screened charge is given by

$$Q_n = Z - \sum_{m<n} p_m \sigma_{nm} - \frac{1}{2} p_n \sigma_{nn} , \tag{9}$$

where the sum is over only the shells interior to the $n^{\text{th}}$ shell and only principal shells are considered.[14]

The values of the first set of coefficients by Mayer, shown in part in Table 45.III(a), are very close to the more recent values of More, shown in part in Table 45.IV(a). The latter were obtained by fitting the coefficients to known ionization energies. More does not give coefficients for distinct $n,l$ subshells.[14] For the calculations reported here, the coefficient table of More has been split into subshells in direct proportion to the splitting done in going from the first table of Mayer to the second, Table 45.III(b). This new split set is shown in Table 45.IV(b). Mayer's coefficients and prescription give the needed approximate results, but the split More coefficients, used with a particular modification of Eq. (9), give results that are closer to atomic-structure-code results for the chlorine ions of interest. The modifications in the prescription are that the sum in Eq. (7) is taken over subshells, and that one uses

$$Q_{n,l} = Z - \sum_{m<n} \sum_{l'} p_{m,l'} \sigma_{n,l;m,l'} - \frac{1}{2} \sum_{l'} p_{n,l'} \sigma_{n,l;n,l'} \tag{10}$$

instead of Eq. (9). Here, $m$ and $n$ are principal quantum numbers. The additional sum is taken over all the angular momentum values, $0 \leq l' \leq m-1$, of a shell of principal quantum number $m$. In Eq. (10), no distinction is made between subshells $l'$ that are interior or exterior to the subshell $l$.

Table 45.III: Mayer screening coefficients $\sigma_{nm}$ with and without splitting of the principal subshells.[13]

(a)

| $m\backslash n$ | 1 | 2 |
|---|---|---|
| 1 | 0.6250 | 0.9383 |
| 2 | 0.2346 | 0.6895 |
| | | |

(b)

| $m\backslash n$ | 1s | 2s | 2p |
|---|---|---|---|
| 1s | 0.6250 | 0.8395 | 0.9712 |
| 2s | 0.2099 | 0.6016 | 0.6494 |
| 2p | 0.2428 | 0.6494 | 0.7266 |

TC2911

Table 45.IV: Splitting of More screening coefficients $\sigma_{nm}$[14] according to the subshell splitting of Mayer.[13]

(a)

| $m\backslash n$ | 1 | 2 |
|---|---|---|
| 1 | 0.3125 | 0.9380 |
| 2 | 0.2345 | 0.6038 |
| | | |

(b)

| $m\backslash n$ | 1s | 2s | 2p |
|---|---|---|---|
| 1s | 0.3125 | 0.8392 | 0.9709 |
| 2s | 0.2098 | 0.5268 | 0.5678 |
| 2p | 0.2427 | 0.5679 | 0.6363 |

TC2912

Equation (10) does give improved approximate agreement for L-shell chlorine ions, compared with results obtained with the Mayer prescription, which justifies its use for other elements near chlorine, e.g., from silicon through calcium. Nevertheless, extending More's prescription to separate $n,l$ subshells beyond the neighborhood of L-shell chlorine ions deserves a careful and truly comprehensive treatment, which has not been done here.

Using the energies of L-shell states obtained from the modified More prescription, correction factors for the carbon-like species of silicon, chlorine, and calcium are evaluated from Eq. (6) and plotted in Fig. 45.17. The changes in the correction curves for the other species are very similar. The dotted line is the carbon-like chlorine curve from Fig. 45.16, which was derived using average excitation energies from the atomic-structure code.[10] The close agreement between the two chlorine curves shows that the use of the modified screening prescription is adequate for this purpose. As the nuclear charge changes by about 50%, over the range of elements from silicon ($Z = 14$) through calcium ($Z = 20$), the correction curve shifts in temperature by less than a factor of 2. Other than this displacement in temperature, which reflects the change in the 2s–2p excitation energy, the curves are very similar.

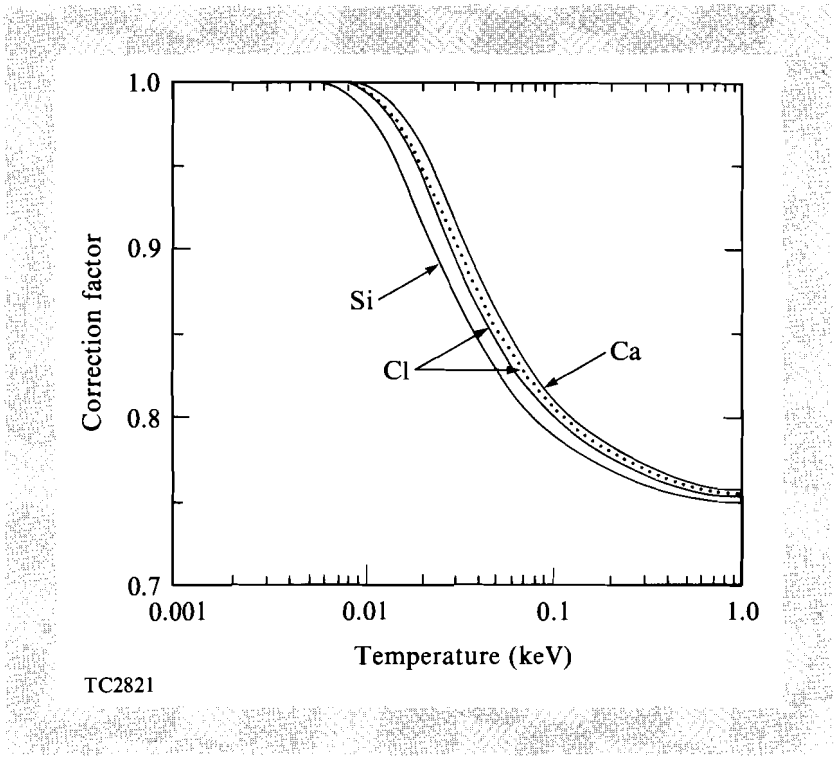


Fig. 45.17
The temperature-dependent absorption correction factor changes relatively little over the range of elements from silicon through calcium, as is shown here for the carbon-like species. Excitation energies used to calculate the solid curves were obtained using the screened hydrogenic approximation. The dotted line is the carbon-like chlorine curve from Fig. 45.16, which was derived from average excitation energies obtained using results from the atomic-structure code.[10]

**Scaling of Absorption Strengths**

To illustrate the distribution and relative strengths of the 1s–2p transitions of the L-shell ionization species, Fig. 45.18 shows an artificial chlorine spectrum where the lines represent the contribution of each initial configuration to the average oscillator strength of all the 1s–2p transitions of each ionization species. The averaging over each species is done with respect to the statistical weight of the initial state of each individual transition. The species are helium-like through fluorine-like, and the three possible initial configurations are $1s^2 2s^2 2p^n$ (ground), $1s^2 2s 2p^{n+1}$ (singly excited), and $1s^2 2p^{n+2}$ (doubly excited), subject to the restriction that there be no more than six 2p electrons in the final state. Lines are positioned at the average transition energy for the initial configuration they represent. The mean array energies from the initial configurations of a given species are closely spaced, as is also apparent in Fig. 45.15. These results have been obtained from detailed numerical atomic-structure calculations.

The crosses in Fig. 45.18 are configuration-averaged absorption strengths that have been scaled from the helium-like absorption strength in Table 45.II, assuming that they scale with the square of the transition energy and with the vacancy fraction of the initial 2p subshell. The relative strengths of the configuration averages within each species agree extremely well, and the agreement in general is reasonably good. A small adjustment in the assumed transition-energy scaling would compensate for most of the discrepancy. Even though the spectator charge in these ions varies from 1e to 8e (nearly half the nuclear charge, in the case of chlorine), this scaling is seen to account for nearly all the variation in the average absorption strength from configu-

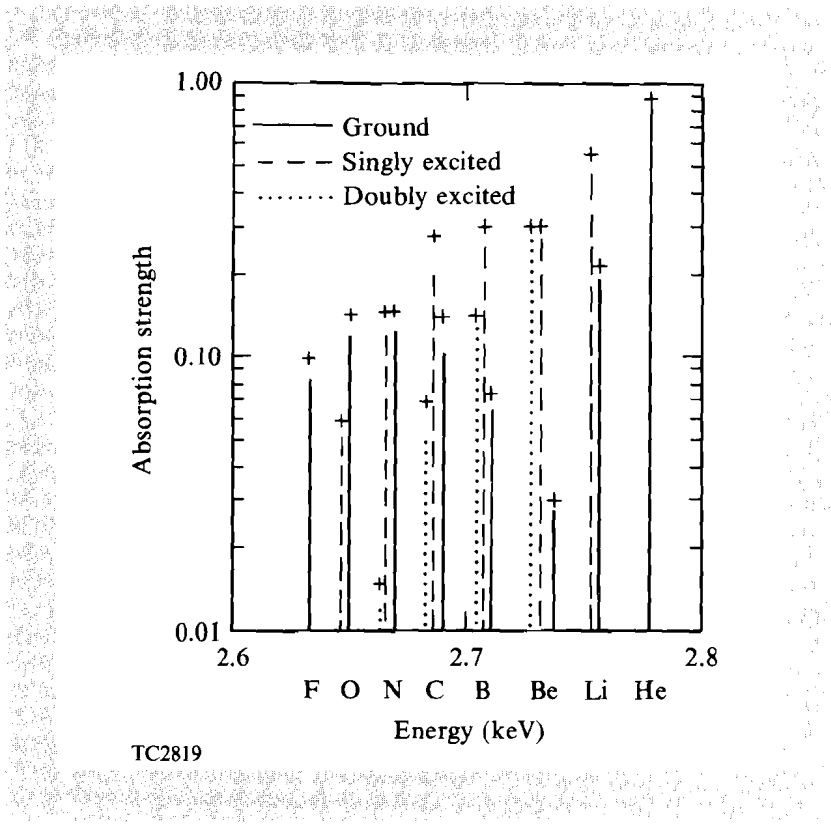


Fig. 45.18
This artificial spectrum is a plot of the average 1s–2p absorption strengths of the possible initial configurations of the helium-like through fluorine-like ionization species of chlorine. Lines are positioned at the average transition energies. The crosses are values scaled from the helium-like absorption strength given in Table 45.II. Scaling with the square of the transition energy and with the vacancy fraction of the initial 2p subshell is seen to account for nearly all of the changes in the average absorption strength.

ration to configuration and from species to species. In particular, the absorption strengths for each initial configuration in any species do indeed occur in very close proportion to their respective 2p vacancy fractions, consistent with the assumption used in evaluating Eq. (6). This scaling is illustrated for the specific case of chlorine, but it can be expected to apply comparably well to the L-shell species of other elements in the neighborhood of chlorine.

## Conclusions and Summary

In calculating the line opacity of shell material for the purpose of absorption spectroscopy, most of the absorption can be due to states in excited, and even doubly excited configurations. The temperature-dependent thermal partition of ions into excited configurations results in the temperature dependence of the strengths of the absorption bands. The effect of the excited configurations on the average absorption strength of each species can lead to areal densities underestimated by as much as 33%, if they are not taken into account. Even though other effects, such as inhomogeneities in temperature and density and the nonuniform sampling of the shell by a compact continuum source, can introduce comparable uncertainties and ambiguities into estimates of areal densities, the effect of the excited configurations is systematic and should not be neglected.

This article describes in general terms the effects of these excited configurations, not only as a point of scientific interest, but as a means of

putting into proper perspective the important earlier work that omits these configurations.[2] Since the effects of these excited configurations have been shown to be modest, this article serves to validate this earlier work to within reasonable limits.

ACKNOWLEDGMENT

This work was supported by the U.S. Department of Energy Division of Inertial Fusion under agreement No. DE-FC03-85DP40200 and by the Laser Fusion Feasibility Project at the Laboratory for Laser Energetics, which has the following sponsors: Empire State Electric Energy Research Corporation, New York State Energy Research and Development Authority, Ontario Hydro, and the University of Rochester.

REFERENCES

1. B. Yaakobi, R. L. McCrory, S. Skupsky, J. A. Delettrez, P. Bourke, H. Deckman, C. F. Hooper, and J. M. Soures, *Opt. Commun.* **34**, 213 (1980); A. Hauer, in *Spectral Line Shapes*, edited by B. Wende (W. de Gruyter & Co., Berlin, 1981); D. K. Bradley, J. D. Hares, and J. D. Kilkenny, Rutherford-Appleton Laboratory, Annual Report No. RL-83-043, 1983, p. 5.4.
2. A. Hauer, R. D. Cowan, B. Yaakobi, O. Barnouin, and R. Epstein, *Phys. Rev. A* **34**, 411 (1986).
3. LLE Review **24**, 169 (1985).
4. C. Fievet, Thèse de Doctorat, Paris XI University, Orsay, France, 1989.
5. S. J. Davidson *et al.*, *Appl. Phys. Lett.* **52**, 847 (1988).
6. C. Chenais-Popovics *et al.*, *Phys. Rev. A* **40**, 3194 (1989). Further details of this work are described in Ref. 4.
7. R. C. Mancini and C. F. Hooper, *Rev. Sci. Instrum.* (in press); private communication.
8. R. S. Craxton, R. L. McCrory, and J. M. Soures, *Sci. Am.* **255**, 68 (1986).
9. C. Bauche-Arnoult, J. Bauche, and M. Klapisch, *J. Opt. Soc. Am.* **68**, 1136 (1978).
10. M. Klapisch, *Comp. Phys. Comm.* **2**, 239 (1971); M. Klapisch, J. L. Schwob, B. S. Fraenkel, and J. Oreg, *J. Opt. Soc. Am.* **67**, 148 (1977).
11. J. Balmer *et al.*, *Phys. Rev. A* **40**, 330 (1989).
12. J. C. Slater, *Phys. Rev.* **36**, 57 (1930).
13. H. Mayer, Los Alamos Scientific Laboratory Report AECD-1870 (LADC-464), 1947, decl. 1948.
14. R. M. More, *J. Quant. Spectrosc. Radiat. Transfer* **27**, 345 (1982).
15. R. Marchand, S. Caille, and Y. T. Lee, *J. Quant. Spectrosc. Radiat. Transfer* **43**, 149 (1990).
16. G. C. Pomraning, *The Equations of Radiation Hydrodynamics* (Pergamon, New York, 1973).

# Section 2
# ADVANCED TECHNOLOGY DEVELOPMENTS

## 2.A Application of KTP Crystal as an Electro-Optic Amplitude Modulator

Potassium titanyl phosphate ($KTiOPO_4$ or KTP) has become a widely used nonlinear optical crystal because of its superior properties for several nonlinear-optical applications[1] and, in particular, for second-harmonic generation of $Nd^{3+}$-based lasers.[2] In addition to its well-recognized characteristics, such as high nonlinear coefficients, high-optical-damage threshold, and low insertion loss, it has been shown that KTP has large electro-optical $r$ coefficients and low dielectric constants.[3] These unique properties of KTP crystal make it an attractive material for various electro-optic (E-O) applications, especially as an E-O Q-switch and switchout device in regenerative amplifiers. There has been a great deal of interest in the development of a high-peak-power, high-repetition-rate laser system,[4,5] which is of great importance for spectroscopic studies in physics, chemistry, and biological science. Despite its proven superior qualities as a doubling crystal for 1-μm-Nd lasers, only a few other applications have been addressed during the decade following the discovery of this material. In this regard, one of the primary limitations in the application of KTP as an E-O device has been the intrinsic birefringence of this crystal group.

This article discusses the use of temperature-tuned birefringence compensation of KTP and the operation of a KTP Pockels cell at repetition rates of up to 30 kHz. The application of this Pockels cell for high-peak-power laser systems and YLF regenerative amplifiers is also discussed. Our measurements of the KTP device performance have shown that it has a

high-polarization-extinction ratio and a low dynamic half-wave voltage and is free from acoustic ringing. All of these properties make it a prospective choice for many extra/intracavity high-repetition-rate electro-optical applications.

KTP is a biaxial crystal with an orthorhombic structure (point group $mm^2$). The crystallographic directions $a,b,c$ correspond to the optic axes $x,y,z$, with $c$ being the polar axis. The KTP crystal used in this work was grown using the hydrothermal technique and was cut normal to the principle crystal axes with dimensions $4\times8\times4\ mm^3$ $(x,y,z)$. The $y$-faces were optically polished and Ar coated at 1.053 μm, and the electrodes were deposited on the $z$-faces with ~500 Å of sputtered gold. From consideration of KTP's $mm^2$-point symmetry, light-amplitude modulation for a beam propagating along the $y$ axis requires the beam to be polarized 45° relative to the $x$ axis with the electric field along the $z$ (polar axis) direction. Figure 45.19 shows the KTP Pockels-cell layout. The phase retardation $\Gamma$ for light propagation in a KTP crystal of length $l$ is relative to the voltage $V_z = E_z d$ across the electrodes by

$$\Gamma = -\frac{2\pi}{\lambda} l(n_z - n_x) + \frac{\pi}{\lambda} n_z^3 r_{c1} V \frac{l}{d} , \tag{1}$$

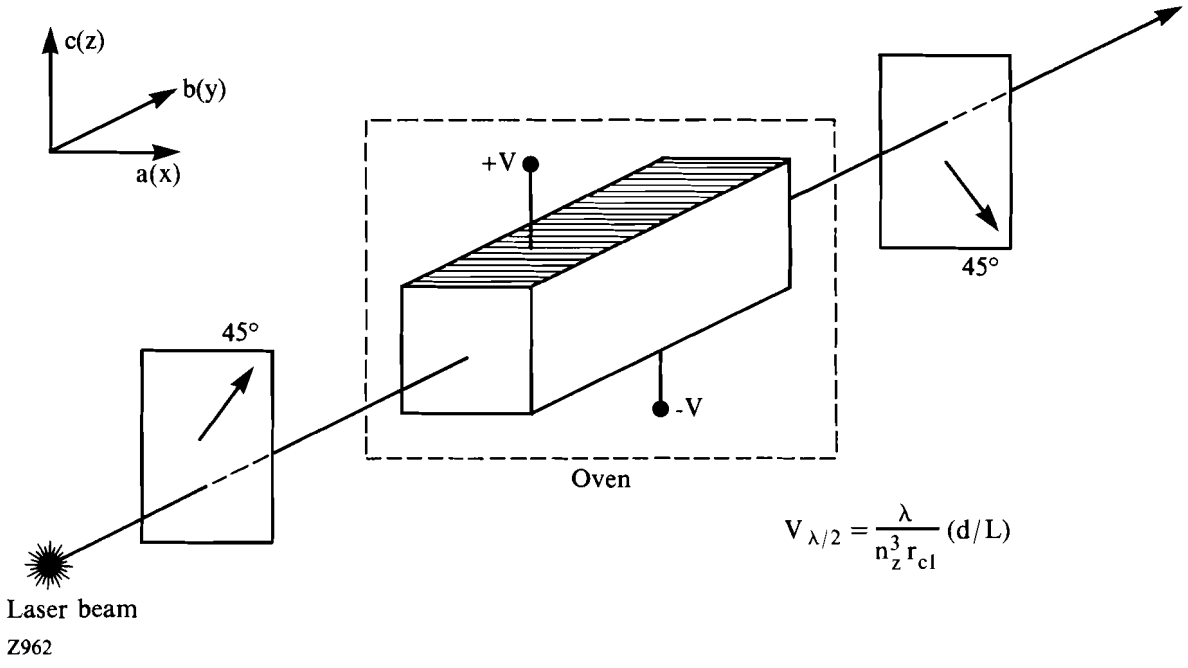


Fig. 45.19
KTP amplitude modulator (Pockels cell) configuration. The crystal is housed in a temperature-controlled oven, and a transverse field is applied along the $z$ axis of the crystal.

where $r_{c1} = r_{33} - (n_1/n_3)^3 r_{13}$ is the effective E-O coefficient for amplitude modulation in the $y$ direction. It is important to note that the first term is in fact an arbitrary static birefringence of the crystal, and it has to be compensated for. The conventional method of compensation, in which a $\lambda/4$ wave plate is placed behind the KTP in the double-pass scheme,[6] is not proper for E-O application as it compensates for both static- and electric-field-induced retardation.

Here we report the compensation for the static birefringence by tuning the KTP crystal temperature. This approach takes advantage of the thermal index of refraction changes ($\Delta n_x = 1.1 \times 10^{-5}\ °C^{-1}$, $\Delta n_z = 1.6 \times 10^{-5}\ °C^{-1}$) and the thermal expansion ($\alpha_y = 0.9 \times 10^{-5}\ °C^{-1}$) of KTP.[1] With the temperature dependence included, the static, field-independent, birefringence term in Eq. (1) can be written

$$\Gamma_{\text{static}} = -\frac{2\pi}{\lambda}(l_o + \Delta l)\left[(n_{zo} + \Delta n_2 \Delta T) - (n_{xo} + \Delta n_x \Delta T)\right], \quad (2)$$

i.e.,

$$\Gamma_{\text{static}} = -\frac{2\pi}{\lambda} l_o (n_{zo} - n_{xo})\left[1 + \left(\frac{\Delta n_z - \Delta n_x}{n_{zo} - n_{xo}} + \alpha_y\right)\Delta T\right], \quad (3)$$

where $l_o$, $n_{zo}$ and $n_{xo}$ are values at room temperature, and $\Delta l = \alpha_y l \Delta T$. From Eq. (3) it is obvious that the static birefringence can be temperature tuned to $2n\pi$, so it will have no effect on the modulation.

Assuming the constants used in Eq. (3) are temperature independent, we can easily estimate the period of two adjacent minimums to be $\Delta T = 13°C$ ($\lambda = 0.633\ \mu m$). Experimental studies of the temperature dependence of the crystal birefringence are shown in Fig. 45.20. For these studies, the KTP Pockels cell was housed in a temperature-controlled oven with 0.1°C sensitivity. The temperature-tuning measurements were done using a HeNe laser with a PMT detector, while the KTP Pockels cell was placed between two crossed calcite polarizers. Compensation for the crystal birefringence is achieved at temperature intervals of 12°C, which is in good agreement with the calculated value. At this point, the contrast ratio is ~2000:1 (limited by the polarizers). This contrast ratio is sufficient for most laser applications and demonstrates the high degree of compensation possible using this simple approach.

At a wavelength of $\lambda = 1.053\ \mu m$ the effective E-O coefficient is $r_{c1} = 28.6$ pm/V for a dc field (low frequency) and 27.0 pm/V for a fast-pulsed field (i.e., high frequency).[3] The theoretical half-wave voltage obtained from the second term of Eq. (1) for our sample crystal size of $4 \times 8 \times 4\ mm^3$ is 2900 V and 3200 V, respectively. Measurements of the half-wave voltage of this KTP crystal were accomplished using a 100-MHz, mode-locked, YLF laser. A synchronized 10-ns, high-voltage electric pulse is applied to the crystal from a microwave triode-based driver to switch out one of the pulses in the 100-MHz pulse train after the second polarizer. An experimental half-wave

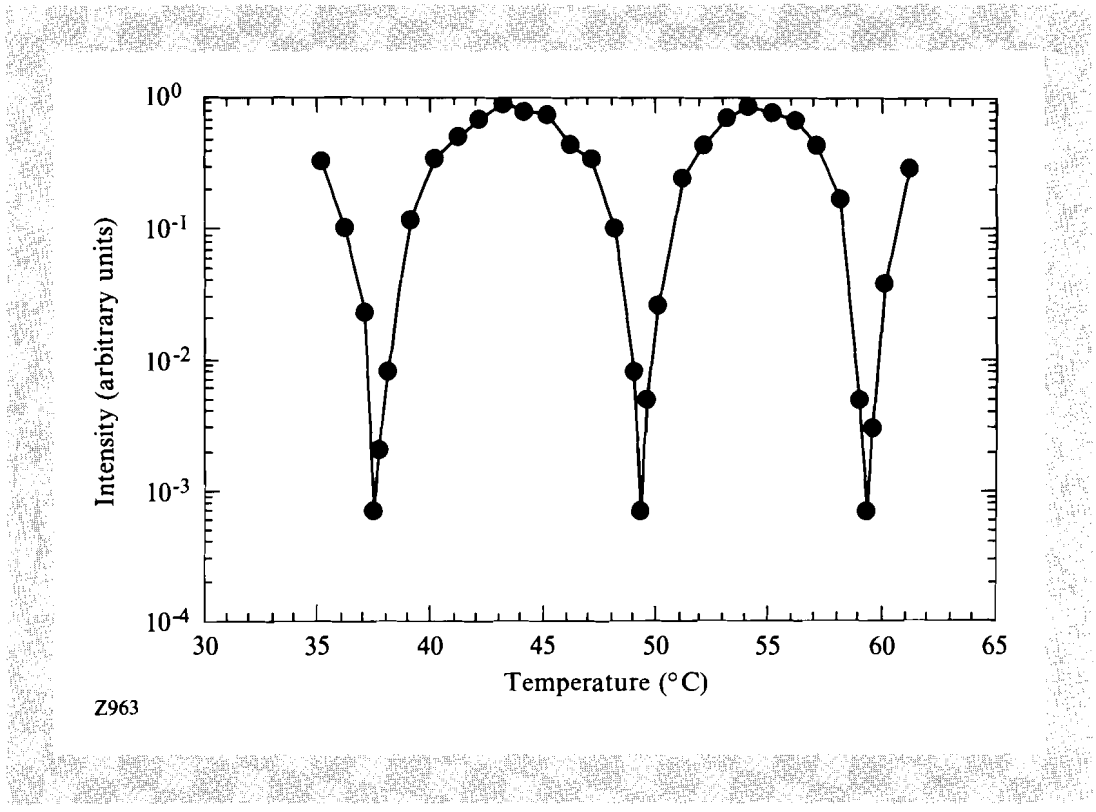


Fig. 45.20
Transmission versus temperature of the KTP Pockels cell sandwiched between crossed polarizers in the absence of an electric field at $\lambda = 633$ nm.

voltage of 3200 V is obtained with 99% single-pulse switchout, confirming the theoretical value. This is about the same as the dc half-wave voltage of a typical $9 \times 9 \times 25$ $mm^3$-$LiNbO_3$ crystal, but 30% to 40% less than the dynamic half-wave voltage of $LiNbO_3$.[7] The dynamic half-wave voltage is the important criteria for Q-switch applications. In addition, the acoustically induced birefringence generated through piezoelectric coupling during the applied field was found to have an insignificant effect on the performance of the KTP Pockels cell (Fig. 45.21). Based on both low half-wave voltage and lack of piezoelectric-induced parasitics, we have successfully demonstrated the operation of this KTP Pockels cell, working up to a 30-kHz repetition rate, limited only by our 10 kV/10 mA-HV power supply.

One of the motivations for this work was to find an alternative material to replace the commonly used $LiNbO_3$ Pockels cell. $LiNbO_3$ crystal has several drawbacks, such as strong acoustic ringing and a moderate-optical-damage threshold when used as an intracavity device. Our work has shown KTP to be a strong candidate for the high-peak-power, high-repetition-rate application. To demonstrate this, a KTP Pockels cell was used as a cavity dumper for regenerative pulse amplification and Q-switch operation of a YLF resonator. In regenerative pulse amplification, the pulse output was limited to 0.5 mJ at a 2.5-kHz repetition rate by the crystal aperture. In this mode of

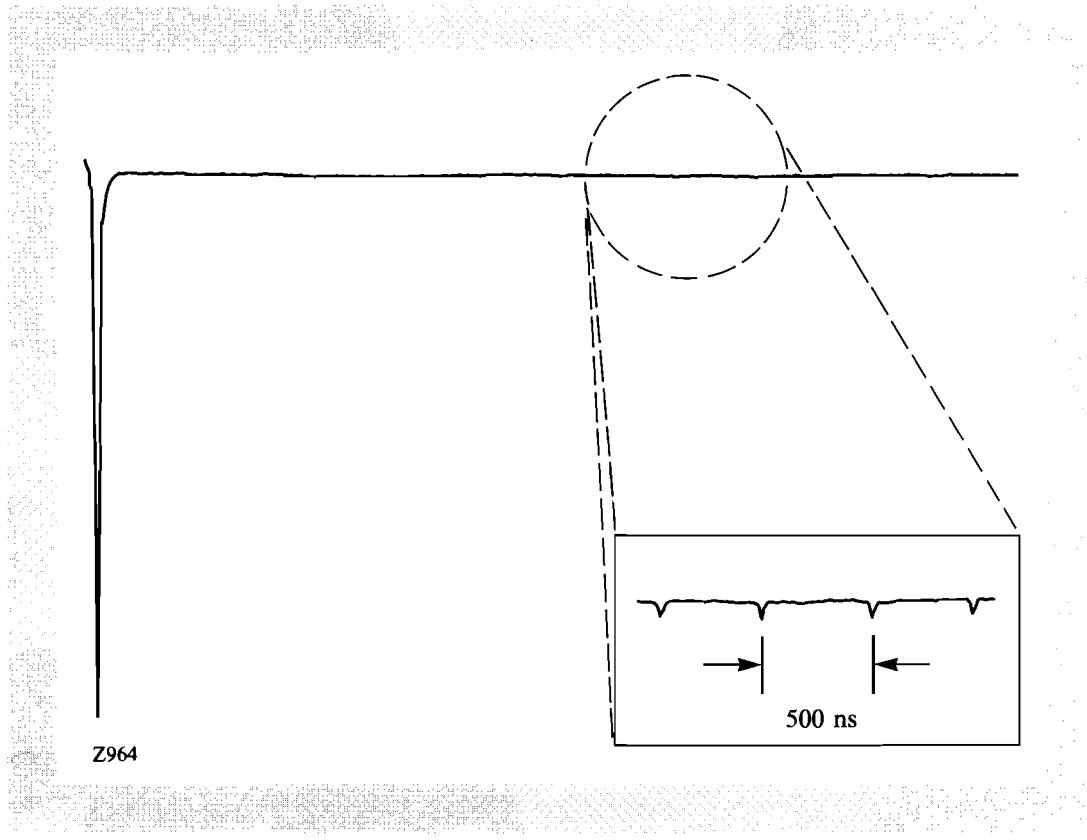


Fig. 45.21
Single-pulse switchout from a 100-MHz pulse train at 1053 nm. The almost complete absence of acoustic ringing is evident from the insert.

operation, the crystal developed some thermal-lensing problems. The thermal lensing did not have a significant effect on the output power but did affect the stability of the laser. This problem should be reduced by using low-temperature, hydrothermally grown crystals that have fewer defects than the high-temperature-grown crystal used in this study.

In conclusion, we have developed a temperature-tuned birefringence-compensated KTP Pockels cell capable of working at a tens-of-kilohertz repetition rate. Applications of this device for high-peak-power, high-repetition-rate Q-switching and regenerative-pulse amplification have also been demonstrated. Our work has shown that KTP has promising potential for various E-O modulation applications other than its major role as a doubling crystal.

## ACKNOWLEDGMENT

This work has been supported by NSF grant ECS-860569 and an NSF Presidential Young Investigator award. We gratefully acknowledge support from the Alfred P. Sloan and Henry Dreyfus Teacher-Scholar Fellowships, and we acknowledge stimulating discussion with J. D. Bierlein.

REFERENCES

1. J. D. Bierlein and H. Vanherzeele, *J. Opt. Soc. Am. B* **6**, 622 (1989).
2. R. F. Belt, G. Gashurov, and Y. S. Liu, *Laser Focus* **21**, 110 (1985).
3. J. D. Bierlein and C. B. Arweiler, *Appl. Phys. Lett.* **49**, 917 (1986).
4. X. D. Wang, P. Basseras, R. J. D. Miller, J. Sweetser, and I. A. Walmsley, *Opt. Lett.* **15**, 839 (1990).
5. M. Saeed, D. Kim, and L. F. DiMauro, *Appl. Opt.* **29**, 1752 (1990).
6. K. C. Liu and M. G. Cohen, in *Proceedings of Conference on Lasers and Electro-Optics*, Optical Society of America, Baltimore, MD, 24–28 April 1989.
7. A. S. Bechuk, L. A. Kulevskiy, V. V. Smirnov, and Y. N. Solovyeva, *Radio Eng. Electron. Phys. (USSR)* **14**, 919 (1969).

## 2.B Nonresonant $\chi^{(3)}_{1111}$ Obtained by Nearly Degenerate Four-Wave Mixing Using Chirped-Pulse Technology

Optical nonlinear effects based on the third-order susceptibility $\chi^{(3)}$ are often investigated by four-wave-mixing techniques. Starting with the classic 1965 proof-of-principle experiments by Maker and Terhune,[1] these measurements have yielded $\chi^{(3)}$ values for many condensed compounds. When these measurements are carried out in a fully degenerate manner, i.e., when $\chi^{(3)}_{ijkl}(-\omega, \omega, \omega, -\omega)$ is probed, the experimental hardware requirements become simple and relatively inexpensive, thereby permitting the widespread use of the technique. In a more complicated embodiment using excitation beams of two frequencies, $\omega_1$ and $\omega_2$, and $\omega_1 > \omega_2$, four-wave mixing takes on the form of coherent anti-Stokes Raman scattering (CARS) and coherent Stokes Raman scattering (CSRS), generating new frequencies at either $2\omega_1 - \omega_2$ if intensity $I(\omega_1) >> I(\omega_2)$, or at $2\omega_2 - \omega_1$ if the reverse-intensity condition holds and phase-matching requirements are met. Compared to the fully degenerate case, CARS complicates the measurement by requiring two laser sources and by being sensitive to phase matching. The major strength of this technique is that the output signal is both spatially and spectrally separated from the input beams. Whenever $\chi^{(3)}$ magnitudes are anticipated to be low and thus in need of background-free detection, CARS is the method of choice.

Adair, Chase, and Payne[2] have in recent years adopted a nearly degenerate (near 1.06-μm) version of CARS and derived with it the nonlinear refractive index $n_2$ for a large number of optical glasses and crystals. In their approach $\omega_1$ is chosen to differ from $\omega_2$ by no more than $\Delta = 60\ cm^{-1}$, thereby simplifying the phase-matching condition for narrow-bandwidth input beams, $\Delta k = \omega/c\ [2n(\omega) - n(\omega + \Delta) - n(\omega - \Delta)]$. The absence of any significant group-velocity dispersion over a 60-$cm^{-1}$ range in all samples considered guarantees an unprotracted, collinear alignment of all input and output beams for $\Delta k \equiv 0$. We report here on nearly degenerate CARS measurements fashioned after those of Adair, Chase, and Payne,[2] using a novel, all-solid-state, single source for generating picosecond pulses at both $\omega$ and $\omega - \Delta$.

This approach exploits the spectral pulse-shaping ability of the chirped-pulse-amplification technology[3] (CPA). CPA overcomes the intensity-related $B$-integral effects (self-focusing and damage) that limit the amplification of short picosecond pulses in solid-state lasing media. In CPA, short pulses are temporally stretched because of group velocity dispersion (GVD), amplified to higher energies than could be achieved by amplifying the short pulse directly, and then compressed to a short pulse.

In our laser system[4,5] (shown schematically in Fig. 45.22) 50-ps transform-limited pulses are produced at a rate of 100 MHz in a mode-locked Nd:YLF oscillator. These pulses are fed into a 0.8-km, 9-μm core optical fiber where the pulse undergoes self-phase modulation, increasing the frequency bandwidth[6] to ~40 Å and GVD increasing the pulse length to >100 ps. This pulse is further lengthened by an antiparallel double-pass grating pair. At this point, the ~300-ps pulse is amplified in a Nd:glass regenerative amplifier to an energy of ~1 mJ. This pulse is then recompressed to ~1 ps by a double-pass grating pair[7] made up of 1700-lines/mm, gold-coated, holographic gratings. The bandwidth of the amplified pulse is reduced to ~14 Å by gain narrowing in the regenerative amplifier.

The use of an antiparallel, double-pass pair of gratings allows access to the Fourier transform of the laser pulse (in wavelength space). This allows for spectral pulse shaping by the use of appropriate masks.[8] In our case, we use a hard-edge stop $W$ (see Fig. 45.22) to block the central 20 Å of the laser bandwidth. This creates two independent, chirped laser pulses, each with a bandwidth of ~7 Å at ±15 Å from the gain center of the regenerative amplifier. To minimize diffraction effects, a spatial filter before the diffraction gratings is used to place the Fourier transform on a plane exactly at the location of $W$.

These temporally separated pulses are amplified in the regenerative amplifier to an energy of ~0.5 mJ. The symmetry of the injected pulses about the gain center of the regenerative amplifier ensures that the pulses undergo identical amplification and gain narrowing. The resulting pulses each have a bandwidth of 8 Å and are separated by 17 Å.

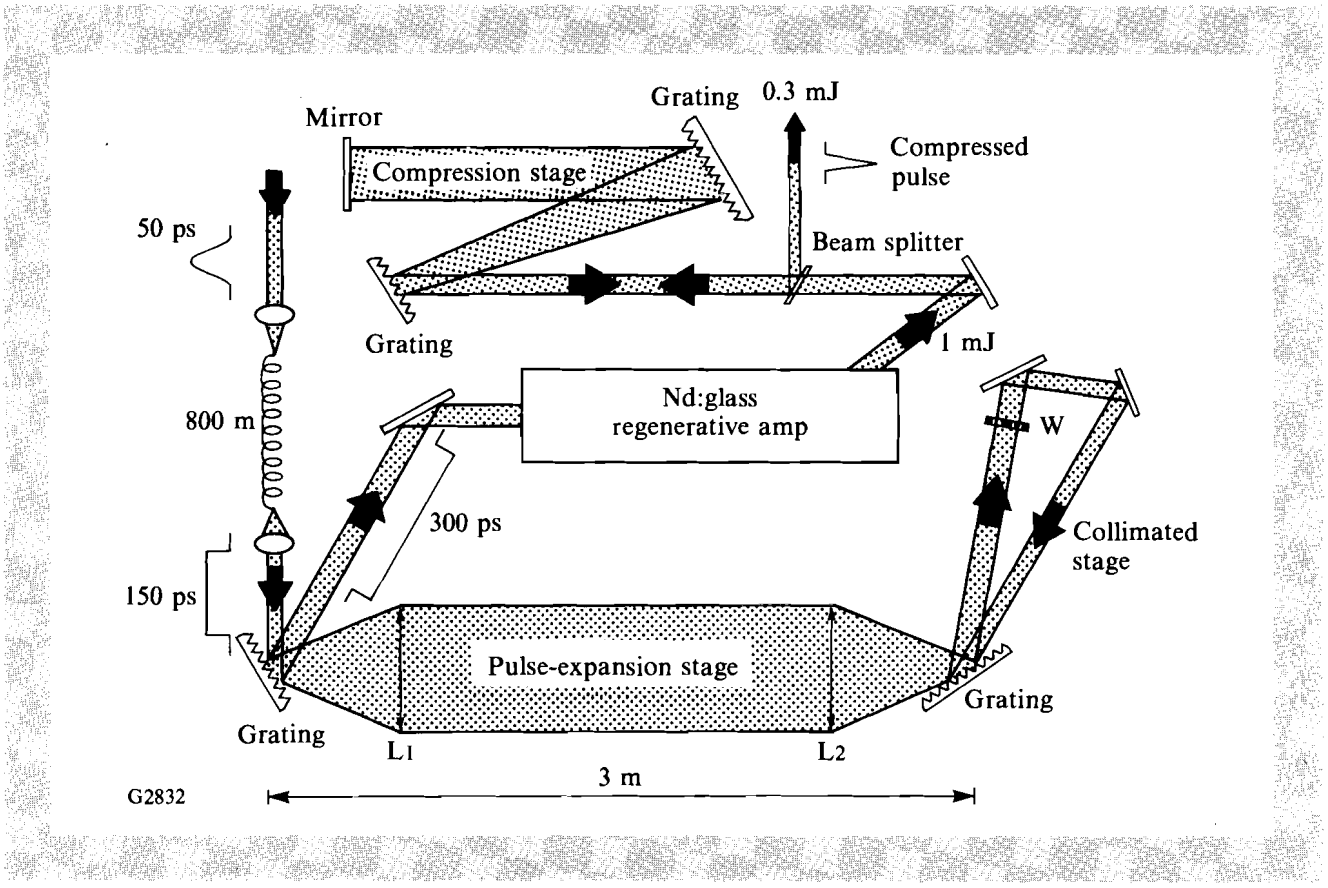


Fig. 45.22
Schematic representation of pulse expansion, spectral windowing, amplification, and pulse compression used in nearly degenerate four-wave-mixing measurements. Using a 50%-output beam splitter after the compression stage can cause feedback into the regenerative amplifier. An improved scheme accomplishes double-pass compression by vertical offset.

Finally, the pulses are spatially filtered and undergo compression in a double-pass, parallel-grating configuration.[7] The autocorrelation of the overlapped pulses is shown in Fig. 45.23. Each of the 75 data points represents a ten-shot average. The 17-Å spectral separation between the two pulses leads to a 2-ps temporal modulation of the combined pulse as expected. This beating must occur for any CARS technique. The envelope of the autocorrelation trace is fitted with a 6.7-ps Gaussian. Because of losses during compression, the pulse reaching the sample carries 0.3-mJ energy.

CARS samples were enclosed in plane-parallel, 0.5-mm-thick cells placed in the converging cone of a 1-m focal-length lens. The beam spot size (0.5 mm) was recorded on calibrated IR film and measured by microdensitometry of the image. The beam exiting the cell, including the $\omega + \Delta$ signal, is recollimated and dispersed by a third double-pass grating pair. The purpose of this grating arrangement is to spatially disperse pump, Stokes, and anti-Stokes signals for a neutral-density filter to attenuate the intense, undepleted signals at $\omega$ and $\omega - \Delta$ to about the signal level of the $\omega + \Delta$, four-

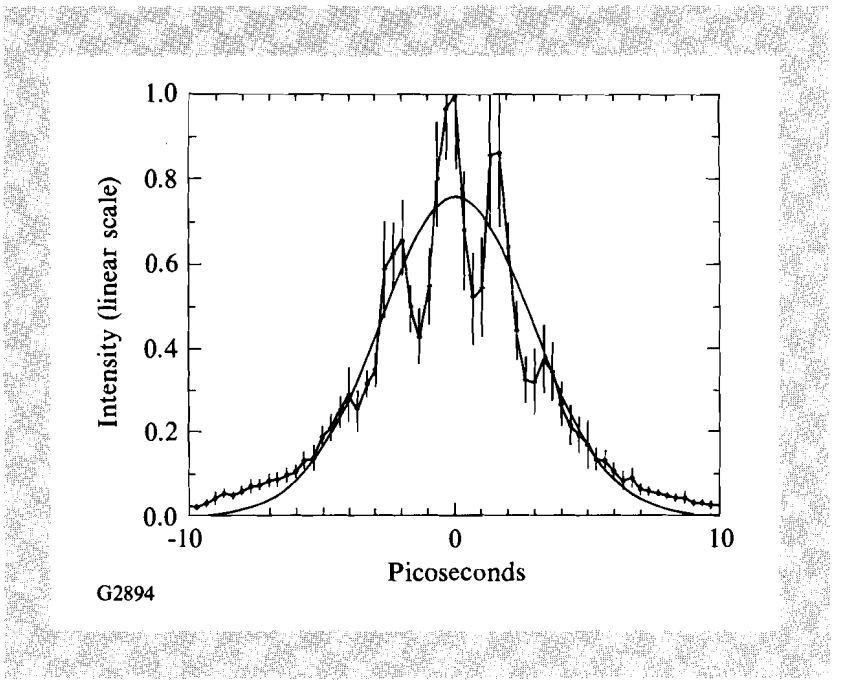


Fig. 45.23
Second-harmonic autocorrelation trace of compressed, spectrally segmented pulse pair. Each data point is a ten-shot average. For comparison, first-order Gaussian (smooth line) is overlayed. The experimentally measured modulation frequency equals the beat frequency between two 17-Å-separated waves.

wave-mixing signal. In this fashion, a cooled, IR-intensified optical multichannel analyzer in the image plane of a monochromator permits recording, within its dynamic-range limits, all signals, $I(\omega)$, $I(\omega - \Delta)$, and $I(\omega + \Delta)$. At the intensity levels prevalent in these measurements, the weaker coherent Stokes four-wave-mixing signal is usually also observed. It appears at $\omega - 2\Delta$ as a result of an interaction of the type $I^2(\omega - \Delta)\, I(\omega)$. Since both $I(\omega)$ and $I(\omega - \Delta)$ have identical polarization, this experiment is probing the tensor component $\chi^{(3)}_{1111}$ of the third-order susceptibility. Figure 45.24 shows the raw-data record of a single-shot measurement on a sample of $CS_2$.

In Fig. 45.25(a) data show single-shot intensities of the anti-Stokes signal as a function of the pump-intensity product $I^2(\omega)\, I(\omega - \Delta)$ for a 0.5-mm $CS_2$ path, while those in Fig. 45.25(b) show the coherent Stokes signal plotted against $I^2(\omega - \Delta)\, I(\omega)$. There is a one-to-one correspondence among data pairs in (a) and (b). The single-shot, systematic-measurement error for these data is smaller than the plotted symbols. In assembling Fig. 45.25 only those measurements were selected for which the spectral width at both $\omega$ and $\omega - \Delta$ fell within a preselected, spectral interval. Fluctuations in the spectral wings from shot to shot contribute to variations in the degree of compression and in the final, temporal pulse shape. We surmise that the prime source for this spectral-width jitter lies in gain-narrowing effects during amplification of the two pulses by the regenerative amplifier. Over the approximately one-order-of-magnitude intensity range plotted along the abscissa in Figs. 45.25(a) and 45.25(b), one finds the expected linear behavior. The solid lines in Fig. 45.25(a) and 45.25(b) are least-square fits to the data points. The non-zero offset at zero input intensity is attributed to both the CARS and Stokes signals riding on pump-pulse wings that have not been deconvoluted (see Fig. 45.24).

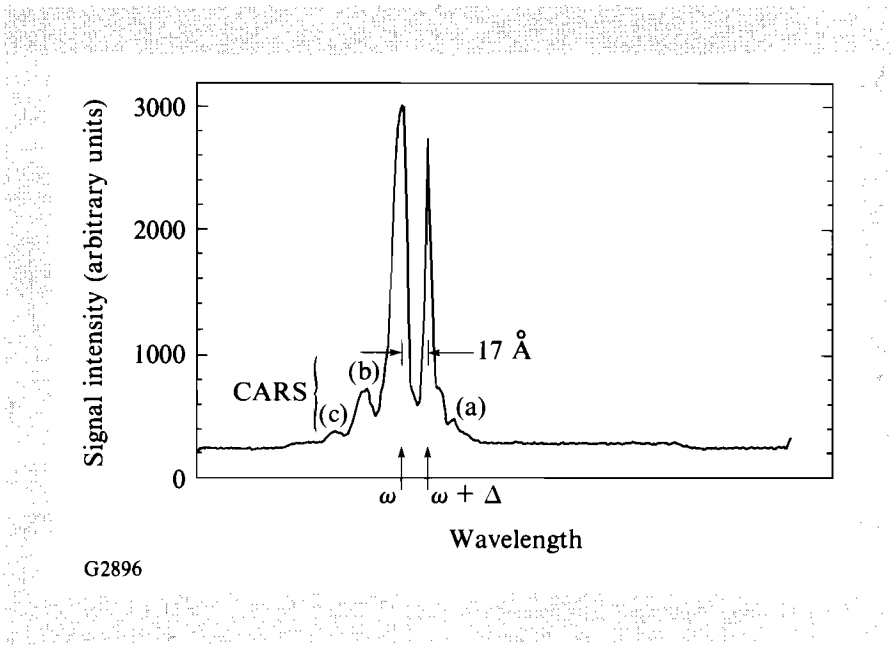


Fig. 45.24
Multichannel detector record from a single-shot, four-wave-mixing event in $CS_2$. Shorter wavelengths are to the left. The central two peaks represent $I(\omega)$ (left) and $I(\omega + \Delta)$ (right). Clearly resolved are the coherent Stokes (a), anti-Stokes (b), and second-order anti-Stokes (c) peaks.

Monitoring all pertinent intensities $I(\omega)$, $I(\omega - \Delta)$, $I(\omega - 2\Delta)$, and $I(\omega + \Delta)$ on every shot facilitates relative sample-to-sample comparison, recording intensity fluctuations, and checking for pump-intensity depletion by the sample. This complete record permits comparing $\chi^{(3)}$ results from different samples with that of a standard such as $CS_2$, without the need for irradiating, on each shot, both the sample and the standard. Of course, care must be taken in placing the samples in identical beam positions. In this manner, we measured the relative third-order susceptibility of several organic compounds. Table 45.V lists the relative CARS and coherent Stokes results normalized to $CS_2$ for nitrobenzene, α-chloronaphthalene, and 4′-octyloxynaphthyl-1′-(4 decyloxybenzoate). In each case the linear refractive index $n$ of the material is accounted for. Refractive indices were measured at 1053 nm on an Abbe refractometer. The last compound is an in-house synthesized liquid crystal out of a series of tolane and ester-linked naphthyl compounds, the nonlinear behavior of which will be published elsewhere. Maintaining alignment throughout the liquid-crystal bulk over the 500-μm sample path was difficult. We chose to measure $\chi^{(3)}$ in the sample's isotropic phase (>90°C), realizing that a penalty in $\chi^{(3)}$ magnitude had to be paid by giving up the macroscopic mesophase alignment. CARS measurements of $\chi^{(3)}$ have been done on liquid-crystalline systems before,[9,10] albeit on different, specific structures. The values for nitrobenzene compare well with the relative value of 0.5 deduced from the 3-ns, four-wave-mixing data of Levenson and Bloembergen.[11] The values for chloronaphthalene can be compared with earlier, relative measurements by Saikan and Marowsky[12]

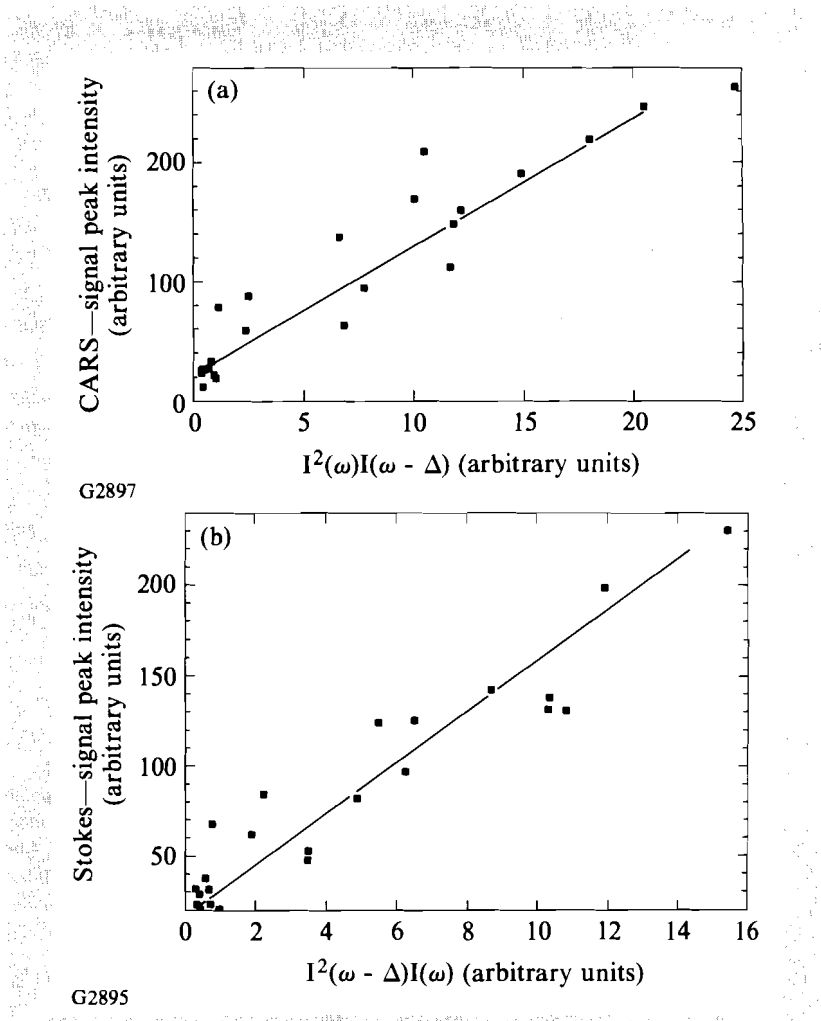


Fig. 45.25
(a) Nonresonant CARS signal magnitude plotted against the input-wave-intensity product $I^2(\omega)I(\omega-\Delta)$. (b) Nonresonant CSRS signal magnitude plotted against the input-wave-intensity product $I^2(\omega-\Delta)I(\omega)$. The data points in (a) and (b) map into each other, i.e., pairs of CARS and CSRS signals were taken simultaneously.

Table 45.V: Measured relative third-order nonlinear susceptibilities $\chi^{(3)}/n^2$.

| Material | $CS_2$ | Nitrobenzene | Chloronaphthalene | OONBOB* |
|---|---|---|---|---|
| CARS | 1 | 0.31±0.07 | 0.46±0.12 | 0.37±0.06 |
| CSRS | 1 | 0.29±0.07 | 0.42±0.10 | 0.39±0.06 |
| *4′-octyloxynaphthyl-1′-(4 decyloxybenzoate) in isotropic phase | | | | |

E5809

who found a relative value of 0.3 for 2-ns excitation near 440 nm. The results show that, within a factor of 2 to 3, these materials approach the $\chi^{(3)}$ values of $CS_2$.

Finally, we mention that this simple and efficient method for generating both $\omega$ and $\omega - \Delta$ allows for several variations. One embodiment takes advantage of the close spectral proximity of Nd emission lines in YAG and YLF (1064 nm versus 1053 nm). By properly synchronizing two, cw mode-locked, Q-switched oscillators[13] one can prepare experimental conditions more elementary than previously described. The major hurdle in this approach is the pulse-to-pulse phase jitter between the two oscillators.[14] Only tight control over jitter assures consistent short-pulse overlap in the sample for acceptable data collection from this third-order nonlinear process. Further experimental simplification can be had by operating a single-gain medium of appropriate bandwidth at two lines simultaneously. In general, any ultrashort pulse source used in conjunction with expansion and compression grating pairs can serve as a driver for this four-wave-mixing experiment.

## ACKNOWLEDGMENT

We thank K. Marshall and B. Puchebner for their effort in sample preparation and T. Gunderman for refractive-index measurements.

This work was supported by the U.S. Army Research Office under contract DAAL03-86-K-0173; the U.S. Department of Energy Division of Inertial Fusion under agreement No. DE-FC03-85DP40200 and by the Laser Fusion Feasibility Project at the Laboratory for Laser Energetics, which has the following sponsors: Empire State Electric Energy Research Corporation, New York State Energy Research and Development Authority, Ontario Hydro, and the University of Rochester.

## REFERENCES

1. P. D. Maker and R. W. Terhune, *Phys. Rev.* **137**, A801 (1965).
2. R. Adair, L. L. Chase, and S. Payne, *J. Opt. Soc. Am. B* **4**, 875 (1987); R. Adair, L. L. Chase, and S. Payne, *Phys. Rev. B* **5**, 3337 (1989).
3. D. Strickland and G. Mourou, *Opt. Commun.* **56**, 219 (1985).
4. P. Maine, D. Strickland, P. Bado, M. Pessot, and G. Mourou, *IEEE J. Quantum Electron.* **QE-24**, 398 (1988).
5. Y.-H. Chuang, S. Augst, H. Chen, J. Peatross, S. Uchida, and D. Meyerhofer, "Suppression of the Pedestal in a Chirped Pulse Amplification Laser" (submitted to *J. Opt. Soc. Am. B*).
6. D. Grischkowsky and A. C. Balant, *Appl. Phys. Lett.* **41**, 1 (1982).
7. E. B. Treacy, *IEEE J. Quantum Electron.* **QE-5**, 454 (1969).
8. A. M. Weiner, D. E. Leaird, J. S. Patel, and J. R. Wullert, *Opt. Lett.* **15**, 326 (1990).

9. A. F. Bunkin *et al.*, *Vestn. Mosk. Univ. Fiz. Astrom. (USSR)* **18**, 35 (1977).

10. L. S. Aslanyan *et al.*, *Opt. Spectrosc.* **53**, 54 (1982).

11. M. D. Levenson and N. Bloembergen, *J. Chem. Phys.* **60**, 1323 (1974).

12. S. Saikan and G. Marowsky, *Opt. Commun.* **26**, 466 (1978).

13. J. M. Bostick, S. A. Mounter, and C. K. Johnson, *Opt. Commun.* **69**, 54 (1988).

14. For an extensive discussion of oscillator phase jitter, see: M. J. W. Rodwell, D. M. Bloom, and K. J. Weingarten, *IEEE J. Quantum Electron.* **QE-25**, 817 (1989).

# Section 3
# NATIONAL LASER USERS FACILITY NEWS

During the first quarter of FY91, several presentations at the November 1990 meeting of the Division of Plasma Physics summarized work done at LLE by user groups from the University of California at Davis, Lockheed Research Laboratory, and the University of Maryland. The work done by principal investigators of NLUF projects continues to be of high caliber and is well received.

**C. F. Hooper** of the University of Florida organized a meeting on the radiation of hot dense matter; data from Ar-filled plastic shells was presented.

A great deal of support continues to be given to **A. Honig's** group at Syracuse University. LLE personnel are designing a new cryogenic shroud to mate with the cold insertion system developed at Syracuse. The first series of target shots with this system are scheduled for calendar year 1991.

The San Francisco office of DOE is formulating the schedule for FY92. Please call their office or the NLUF office at LLE for the deadline for submission of proposals. The steering committee will meet at LLE to review the technical content of the proposals, and their evaluations will be given to DOE for final determination of contract awards.

ACKNOWLEDGMENT

This work was supported by the U.S. Department of Energy Division of Inertial Fusion under agreement No. DE-FC03-85DP40200.

# Section 4
# LASER SYSTEM REPORT

## 4.A GDL Facility Report

During the first quarter of FY91, a regenerative amplifier was built near the GDL oscillator to test concepts for pulse shaping of Gaussian laser pulses. A 100-ps pulse from an oscillator synchronized to the GDL oscillator was used as a seed to the regenerative amplifier. The amplified 100-ps laser pulse is used to drive either a GaAs or Si photoconductive switch. Tests were conducted on GDL to study the time synchronization of the two oscillators, the performance of the photoconductive switches, and the ability to predict the ultimate pulse shape from a model of the electrical characteristics of the switch when connected to a Pockels cell.

There was general system maintenance done of the high-power amplifier section of GDL while the pulse-shaping experiments were being conducted. This included routine amplifier maintenance as well as replacement of several damaged optical elements in spatial filters and up-collimators. GDL will be available for full-system shots during the second quarter of FY91.

ACKNOWLEDGMENT

This work was supported by the U.S. Department of Energy Division of Inertial Fusion under agreement No. DE-FC03-85DP40200 and by the Laser Fusion Feasibility Project at the Laboratory for Laser Energetics, which has the following sponsors: Empire State Electric Energy Research Corporation, New York State Energy Research and Development Authority, Ontario Hydro, and the University of Rochester.

# 4.B OMEGA Facility Report

The OMEGA Laser Facility was used for target experiments, laser development, and driver-line development. OMEGA continues to be used at the rate of 800 to 1200 shots per year. This rate will continue because several OMEGA Upgrade projects will use one or more of OMEGA's beamlines.

The target shots for the first quarter of FY91 were all implosion experiments. CD shells were used as surrogate cryogenic targets to study high-density compression, the implosion of D2-filled plastic shells was studied as a function of SSD bandwidth, and a series of burnthrough targets were used to study implosion stability.

The shot summary for the OMEGA laser this quarter is as follows:

| | | |
|---|---|---|
| Driver line | | 125 |
| Laser test | | 94 |
| Target | | 151 |
| Software | | 7 |
| | TOTAL | 377 |

ACKNOWLEDGMENT

This work was supported by the U.S. Department of Energy Division of Inertial Fusion under agreement No. DE-FC03-85DP40200 and by the Laser Fusion Feasibility Project at the Laboratory for Laser Energetics, which has the following sponsors: Empire State Electric Energy Research Corporation, New York State Energy Research and Development Authority, Ontario Hydro, and the University of Rochester.

# PUBLICATIONS AND CONFERENCE PRESENTATIONS

## Publications


T. Boehly, R. S. Craxton, R. Epstein, M. Russotto, and B. Yaakobi, "X-Ray Lasing in Thick Foil Irradiation Geometry," *Opt. Commun.* **79**, 57–63 (1990).

S.-H. Chen and M. L. Tsai, "New Thermotropic Chiral Nematic Copolymers Using (1S, 2S, 3S, 5R)-(+)- and (1R, 2R, 3R, 5S)-(-)-Isopinocampheol as Building Blocks," *Macromolecules* **23**, 5055–5058 (1990).

W. R. Donaldson, L. Kingsley, M. Weiner, A. Kim, and R. Zeto, "Electro-Optic Imaging of the Internal Fields in a GaAs Photoconductive Switch," *J. Appl. Phys.* **68**, 6453–6457 (1990).

H. E. Elsayed-Ali and J. W. Herman, "Picosecond Time-Resolved Surface-Lattice Temperature Probe," *Appl. Phys. Lett.* **57**, 1508–1510 (1990).

E. M. Epperlein, "Kinetic Theory of Laser Filamentation in Plasmas," *Phys. Rev. Lett.* **65**, 2145–2148 (1990).

D. Golini and S. D. Jacobs, "Transition Between Brittle and Ductile Mode in Loose Abrasive Grinding," *Advanced Optical Manufacturing and Testing* (SPIE, Bellingham, WA, 1990), Vol. 1333, pp. 80–91.

P. A. Jaanimagi and C. Hestdalen, "Streak Camera Phosphors: Response to Ultra-Short Excitation," *Ultrahigh- and High-Speed Photography, Videography, Photonics, and Velocimetry '90* (SPIE, Bellingham, WA, 1990), Vol. 1346, pp. 443–448.

A. M. Kadin, P. H. Ballentine, and W. R. Donaldson, "Relaxation Processes in Optically Excited High-Tc Films," *Physica B* **165 & 166**, 1507–1508 (1990).

L. E. Kingsley and W. R. Donaldson, "Electrooptic Imaging of Surface Electric Fields in High-Power Photoconductive Switches," *IEEE Trans. Electron Devices* **37**, 2449–2458 (1990).

J.-C. Lee and S. D. Jacobs, "Design and Construction of 1064-nm Liquid-Crystal Laser Cavity End Mirrors," *J. Appl. Phys.* **68**, 6523–6525 (1990).

P. W. McKenty, C. P. Verdon, S. Skupsky, R. L. McCrory, D. K. Bradley, W. Seka, and P. A. Jaanimagi, "Numerical Modeling of Effects of Power Imbalance on Irradiation Nonuniformities," *J. Appl. Phys.* **68**, 5036–5043 (1990).

C. J. McKinstrie and R. Bingham, "Erratum: 'The Modulational Instability of Coupled Waves' [*Phys. Fluids B* **1**, 230 (1989)]," *Phys. Fluids B* **2**, 3215 (1990).

## Forthcoming Publications

S. H. Batha, D. D. Meyerhofer, A. Simon, and R. P. Drake, "Enhanced Scattering from Laser-Plasma Interactions," to be published in *Physics of Fluids*.

T. Boehly, M. Russotto, R. S. Craxton, R. Epstein, B. Yaakobi, L. B. DaSilva, J. Nilsen, E. A. Chandler, D. J. Fields, B. J. MacGowan, D. L. Matthews, J. H. Scofield, and G. Shimkaveg, "Demonstration of a Narrow Divergence X-Ray Laser in Neon-Like Titanium," to be published in *Physical Review A*.

H. C. Chen, G. Mourou, and R. Knox, "Time-Resolved Electron Diffraction from Pulse-Excited Crystalline Gold Films," to be published in the *Proceedings of 1989 Materials Research Society Fall Meeting: Beam-Solid Interactions*, Boston, MA, 27 November–2 December 1989; and in *Physical Review Letters*.

P. C. Cheng, V. H-K. Chen, H. G. Kim, and R. E. Pearson, "A Real-Time EPI-Fluorescent Confocal Microscope," to be published in *Journal of Microscopy*.

P. C. Cheng, V. H-K. Chen, H. G. Kim, and R. E. Pearson, "An EPI-Fluorescent Spinning-Disk Confocal Microscope," to be published in the *Proceedings of the 47th Annual Meeting of Electron Microscopy Society of America (EMSA)*, Austin, TX, 14–18 August 1989.

Y.-H. Chuang, Z.-W. Li, D. D. Meyerhofer, and A. W. Schmid, "Nonresonant $\chi^{(3)}_{1111}$ Obtained by Nearly-Degenerate Four-Wave Mixing Using Chirped-Pulse Technology," to be published in *Optics Letters*.

J. Delettrez and E. Epperlein, "Comments on 'Modified Nonlocal Heat-Transport Formula for Steep Temperature Gradients'," to be published in *Physics Review A*.

J. Delettrez, R. Epstein, D. K. Bradley, P. A. Jaanimagi, R. C. Mancini, and C. F. Hooper, "Hydrodynamic Simulations, with Non-LTE Atomic Physics,

of High-Density Implosions of Argon-Filled Polymer Shell Targets," to be published in the *Proceedings of the 1990 International Workshop on Radiative Properties of Hot Dense Matter*, Sarasota, FL, 22–26 October 1990.

W. R. Donaldson and L. E. Kingsley, "Optical Probing of Field-Dependent Effects in GaAs Photoconductive Switches," to be published in the SPIE's *Proceedings of a Symposium on Laser Science and Optical Applications*, Boston, MA, 4–9 November 1990.

H. E. Elsayed-Ali, T. Juhasz, G. O. Smith, and W. E. Bron, "Femtosecond Thermoreflectivity and Thermotransmissivity of Polycrystalline and Single-Crystalline Gold Films," to be published in *Physical Review B*.

E. M. Epperlein, "Electron Kinetics in Laser-Driven Inertial Confinement Fusion," to be published in the *Proceedings of the Topical Conference on Research Trends in Nonlinear and Relativistic Effects in Plasmas*, La Jolla, CA, 5–8 February 1990.

## Conference Presentations

A. Schmid, S. Papernov, Z.-W. Li, K. Marshall, T. Gunderman, J.-C. Lee, M. Guardalben, and S. D. Jacobs, "Liquid-Crystal Materials for High Peak-Power Laser Applications," 3rd International Topical Meeting on Optics of Liquid Crystals, Cetraro, Italy, 1–5 October 1990.

R. L. McCrory, J. M. Soures, J. Knauer, S. Letzring, F. J. Marshall, S. Skupsky, W. Seka, C. Verdon, D. Bradley, R. S. Craxton, J. Delettrez, R. Epstein, P. Jaanimagi, R. Keck, T. Kessler, H. Kim, R. Kremens, P. W. McKenty, R. Short, and B. Yaakobi, "Direct-Drive Implosion Experiments at the Laboratory for Laser Energetics," Thirteenth International Atomic Energy Agency Conference on Plasma Physics and Controlled Nuclear Fusion Research, Washington, DC, 1–6 October 1990.

---

The following presentations were made at the SPIE CAN-AM Eastern '90; Session IV: Components and Systems: Design, Manufacturing & Testing, Rochester, NY, 4–5 October 1990:

D. Golini and S. D. Jacobs, "Brittle and Ductile Mode Loose Abrasive Grinding: An Examination of Surface Stresses in ULE."

T. E. Gunderman, "Liquid Crystal Optics: Polarizers, Isolators and Waveplates."

W. Seka, D. Golding, B. Klein, R. J. Lanzafame, and D. Rogers, "Laser Energy Repartition Inside Metal, Sapphire, and Quartz Surgical Laser Tips."

---

H. Kim, M. D. Wittman, J. M. Soures, P. C. Cheng, R. S. Acharya, T. H. Liu, and J. Samarubandu, "Characterization of Inertial Fusion Targets with Confocal Microscopy," presented at the 37th Annual AVS Symposium & Topical Conference, Toronto, Canada, 8–12 October 1990.

---

The following presentations were made at the International Workshop on Radiative Properties of Hot Dense Matter, Sarasota, FL, 22–26 October 1990:

J. Delettrez, R. Epstein, D. K. Bradley, P. A. Jaanimagi, R. C. Mancini, and C. F. Hooper, "Hydrodynamic Simulations, with Non-LTE Atomic Physics, of High-Density Implosions of Argon-Filled Polymer Shell Targets."

P. A. Jaanimagi, D. K. Bradley, J. Delettrez, F. Marshall, R. C. Mancini, and C. F. Hooper, "Implosion of Argon-Filled Polymer Shell Targets: Experimental Aspects."

---

The following presentations were made at the OSA Annual Meeting, Boston, MA, 4–9 November 1990:

M. J. Guardalben, S.-G. Wang, J. Landry, and N. George, "Time-Resolved Study of Smectic A Guest-Host System Response to 488 nm Pulsed Excitation Using Laser Speckle."

J. A. Hawthorne, S. N. Houde-Walter, S. Papernov, and A. W. Schmid, "Properties of Sputtered Glass Films for Waveguide Applications."

M. S. Jin, D. J. Smith, A. Schmid, and S. Papernov, "Ultraviolet Properties of $Y_2O_3$ and $ZrO_2$ Films Produced under Various Ion-Assisted Deposition Conditions."

T. Kessler, "Issues in Pulsed Laser Interferometry and Coherence Control" (tutorial).

A. Schmid, K. Marshall, B. Puchebner, Z.-W. Li, Y. H. Chuang, and D. Meyerhofer, "Third-Order Nonlinear Susceptibility at 1053 nm of a Series of Ester- and Tolane-Linked, Liquid-Crystal Naphthyl Compounds."

M. D. Skeldon and R. Bahr, "Stimulated Rotational Raman Scattering in Air with a High-Power Broadband Laser."

D. J. Smith, M. S. Jin, and Z. R. Chrzan, "High Contrast Thin Film Polarizers for Nd:Glass Laser Systems."

---

W. R. Donaldson and L. E. Kingsley, "Optical Probing of Field-Dependent Effects in GaAs Photoconductive Switches," presented at the SPIE Symposium on Laser Science and Optical Applications, OE/Boston '90, Boston, MA, 4–9 November 1990.

---

The following presentations were made at the Thirty-Second Annual Meeting, Division of Plasma Physics (APS), Cincinnati, OH, 12–16 November 1990:

R. Bahr, W. Seka, R. S. Craxton, D. Bradley, P. Jaanimagi, D. Meyerhofer, and J. M. Soures, "Diagnosing Long-Scale Length Interaction Experiments on OMEGA."

T. Boehly, M. Russotto, B. Yaakobi, R. Epstein, R. S. Craxton, B. MacGowan, L. DaSilva, E. Chandler, J. Nilsen, M. Eckart, A. R. Fry, D. Matthews, and G. Shimkaveg, "Demonstration of a Resonantly Photo-Pumped X-ray Laser."

D. K. Bradley, J. Delettrez, P. A. Jaanimagi, and C. P. Verdon, "Burnthrough Measurements on the OMEGA Laser System."

D. L. Brown, T. Kessler, S. Letzring, S. Morse, and R. L. Short, "Laser Propagation Experiments on OMEGA with SSD."

H. Chen, Y. H. Chuang, S. Uchida, D. Bradley, R. Epstein, P. Jaanimagi, B. Yaakobi, and D. D. Meyerhofer, "Studies of X-Ray and EUV Emission From 1 ps Laser-Plasma Interactions."

R. S. Craxton and W. Seka, "The Production of Long-Scale-Length Plasmas on OMEGA."

J. Delettrez, "A Novel Method to Study the Effects of Illumination Uniformity on the Rayleigh-Taylor Instability: Burnthrough Experiments" (invited talk).

J. Delettrez, "Modeling the Burnthrough Experiments with an Interactive Mix Model in *LILAC*."

E. Epperlein, "A Kinetic Theory of Laser Beam Thermal and Ponderomotive Filamentation in Plasmas."

R. Epstein and B. Yaakobi, "Atomic, Radiative, and Kinetic Effects on X-ray Absorption Lines in Inertial-Confinement Experiments."

J. Glanz, M. V. Goldman, D. L. Newman, and C. J. McKinstrie, "Sideband Instabilities and Emission from Counterpropagating Langmuir Pump Waves."

P. A. Jaanimagi, J. Kelly, R. Keck, and W. Seka, "Pulse Shape and Power Balance Measurements on OMEGA."

T. Kessler, T. Boehly, R. S. Craxton, J. Kelly, S. Kumpan, R. L. McCrory, W. Seka, S. Skupsky, J. M. Soures, and C. Verdon, "Target Irradiation Using the OMEGA Upgrade Laser System."

J. P. Knauer, D. K. Bradley, J. Delettrez, P. Jaanimagi, R. Keck, H. Kim, R. Kremens, S. Letzring, F. Marshall, R. L. McCrory, P. McKenty, M. Russotto, W. Seka, S. Skupsky, J. M. Soures, C. Verdon, and B. Yaakobi, "Implosion of D2 Filled Plastic Shells with the OMEGA Laser."

S. Letzring, S. Skupsky, R. Short, R. Epstein, J. P. Knauer, and F. J. Marshall, "Implementation and Initial Experimental Results of 9 GHz SSD on OMEGA."

G. G. Luther, C. J. McKinstrie, and M. V. Goldman, "Two-Dimensional Instabilities of Counterpropagating Light Waves."

F. J. Marshall, C. P. Verdon, J. P. Knauer, D. K. Bradley, R. L. Keck, H. Kim, R. L. Kremens, S. A. Letzring, R. L. McCrory, M. Russotto, and J. M. Soures, "Implosion Experiments on Solid Shell Targets Performed on OMEGA."

C. J. McKinstrie, M. Yu, and G. G. Luther, "Stimulated Raman Forward Scattering and the Relativistic Modulational Instability of Light Waves in Rarefied Plasma."

C. J. McKinstrie, M. V. Goldman, and G. G. Luther, "Two-Dimensional Instabilities of Counterpropagating Light Waves."

D. D. Meyerhofer, D. Bradley, Y.-H. Chuang, H. Chen, J. Delettrez, R. Epstein, P. Jaanimagi, S. Uchida, and B. Yaakobi, "Results From High-Intensity, 1 ps, Laser-Plasma Interaction Experiments."

J. C. Moreno, H. R. Griem, S. Goldsmith, J. S. Wang, and R. Epstein, "Spectral Measurements of Plasma Expansion Velocities Using Spherical Targets."

D. L. Newman, M. V. Goldman, J. Glanz, P. A. Robinson, and C. J. McKinstrie, "Nonlinear Wave Dynamics in a Plasma Driven by Counterpropagating Langmuir Pump Waves."

G. Pien, F. J. Marshall, G. Altmann, and C. Dulnikowski, "X-ray Imaging of Laser Fusion Targets Using Kirkpatrick-Baez (KB) Microscopes."

W. Seka, R. S. Craxton, R. Bahr, D. Bradley, P. Jaanimagi, J. Knauer, S. Letzring, D. Meyerhofer, R. L. Short, A. Simon, and J. M. Soures, "Long-Scale Length Interaction Experiments on OMEGA."

R. W. Short, "The Effect of Refraction on Filamentation."

A. Simon, "Analysis of 90° Brillouin Scattering Experiments."

B. Yaakobi, F. J. Marshall, J. Knauer, and J. M. Soures, "High-Resolution X-Ray Back-Lighting of Spherical Targets."

---

The following presentations were made at the Materials Research Society 1990 Fall Meeting, Boston, MA, 26 November–1 December 1990:

S. Krishnamurthy and S. H. Chen, "Helical Sense and Twisting Power in Thermotropic Side-Chain Copolymers."

L. J. Shaw-Klein, S. J. Burns, and S. D. Jacobs, "Thermal Conductivity of Aluminum Nitride Thin Films."

C. J. Twomey and S. H. Chen, "Complex Formation and Morphology in Neodymium Chloride-Poly(Ethylene Oxide) System."

---

H. E. Elsayed-Ali, J. W. Herman, and K.-K. Lo, "Picosecond Time-Resolved Electron Diffraction Studies of Laser Heated Metals," presented at the International Conference on Lasers 1990, San Diego, CA, 9–14 December 1990 (invited paper).

ACKNOWLEDGMENT

The work described in this volume includes current research at the Laboratory for Laser Energetics, which is supported by Empire State Electric Energy Research Corporation, New York State Energy Research and Development Authority, Ontario Hydro, the University of Rochester, and the U.S. Department of Energy Division of Inertial Fusion under agreement No. DE-FC03-85DP40200.